Baghdadite Coating Formed by Hybrid Water-Stabilized Plasma Spray for Bioceramic Applications: Mechanical and Biological Evaluations

Duy Quang Pham[1,2], Christopher C. Berndt[1,2], Jan Cizek[3], Uwe Gbureck[4], Hala Zreiqat[2,5], Zufu Lu[2,5], Andrew Siao Ming Ang[1,2*]

1. Australian Research Council Training Centre for Surface Engineering for Advanced Materials (SEAM), School of Engineering, Swinburne University of Technology, Hawthorn, Victoria, Australia
2. Australian Research Council Training Centre for Innovative BioEngineering, The University of Sydney, Sydney, New South Wales, Australia
3. Institute of Plasma Physics, The Czech Academy of Sciences, Prague, Czech Republic
4. Department for Functional Materials in Medicine and Dentistry, University of Würzburg, Würzburg, Germany
5. Biomaterials and Tissue Engineering Research Unit, School of Biomedical Engineering, The University of Sydney, Sydney, New South Wales, Australia

Corresponding author:

- E-mail address: aang@swin.edu.au (Andrew Siao Ming Ang)
- Phone: +61 3 9214 4964 | Fax: +61 3 9214 5050
- Postal address:

  Faculty of Science, Engineering and Technology, Swinburne University of Technology H38, PO Box 218 Hawthorn, Victoria 3122, Australia

Highlights

- A Baghdadite coating was produced by hybrid water-stabilized plasma to compare with a commercial hydroxyapatite coating manufactured by atmospheric plasma spray.
- The Baghdadite coating presented significantly better mechanical properties than the hydroxyapatite coating.
- The Baghdadite coating possessed a more uniform microstructure with more consistent distribution of mechanical properties across the thickness comparing with hydroxyapatite coating
- The Baghdadite coating supported the attachment and proliferation of human osteoblasts.
- The Baghdadite presented excellent osteogenic gene expression.

Key words: Baghdadite, Hydroxyapatite, Atmospheric Plasma Spray, Hybrid Water-Stabilized Plasma Spray, Nanoindentation, Mechanical Properties, Cell Viability, Gene Expression, Calcium Silicate Bioceramics.

Abstract

This work studies the mechanical and biological properties of Baghdadite (BAG, $Ca_3ZrSi_2O_9$) coating manufactured on Ti6Al4V substrates by hybrid water-stabilized plasma spray (WSP-H). Hydroxyapatite (HAp, $Ca_{10}(PO_4)_6(OH)_2$) coating was produced by gas-stabilized atmospheric plasma spray and used as a reference material. Upon spraying, the BAG coating exhibited lower crystallinity than the HAp coating. Mechanical testing demonstrated superior properties of the BAG coating: its higher hardness, elastic modulus as well as a better resistance to scratch and wear. In the cell viability study, the BAG coating presented better human osteoblast attachment and proliferation on the coating surface after three days and seven days compared to the HAp counterpart. Furthermore, the gene expression study of human osteoblasts indicated that the BAG coating surface showed higher expression levels of osteogenic genes than those on the HAp coating. Overall, this study indicates that enhanced mechanical and bioactive properties can be achieved for the BAG coating compared to the benchmark HAp coating. It is therefore concluded here that the BAG coating is a potential candidate for coating orthopedic implants.

1. Introduction

Comprised of CaO and SiO_2, calcium silicate-based bioceramics are receiving attention for applications in orthopedic implants due to their encouraging properties of bone bioactivity and biocompatibility [1]. The Ca-Si-based bioceramics are capable of promoting osteogenic differentiation of stem cells such as bone marrow stromal cells, adipose-derived stem cells, human dental pulp cells and periodontal ligament cells [2-5]. Some of the Ca-Si bioceramics that have been explored for orthopedic implant applications include wollastonite ($CaSiO_3$), dicalcium silicate (Ca_2SiO_4) and tricalcium silicate (Ca_3SiO_5) [1]. Bulk wollastonite exhibited bioactive properties by forming an apatite layer on the surface when immersed in simulated body fluid [6]. Similar phenomenon of apatite formation was also found on the surface of a plasma sprayed coating of wollastonite on Ti6Al4V [7]. A larnite (β-Ca_2SiO_4) scaffold with porous structure exceeding 78% of porosity illustrated similar

ability in forming apatite layers [8]. Despite these advantages, a major concern of the Ca-Si bioceramics is the rapid dissolution that would diminish the stability and eventually lead to disintegration within the host body. As the result, the service time of the implant may be decreased due to a reduction of both the bond strength as well as fixation of the implant. The dissolution behavior and stability of Ca-Si-based bioceramics has been improved by doping with metals or metal oxides such as zirconium (Zr), strontium (Sr), zinc (Zn) and aluminum (Al); these have further triggered improvements in the mechanical properties as well as biological properties [9].

A zirconium-incorporated Ca-Si-based bioceramic named Baghdadite (BAG) with the formula of $Ca_3ZrSi_2O_9$ has been recognized as a promising candidate for applications of orthopedic implants [10]. BAG in its bulk form presented excellent osseointegration and the presence of zirconium did not induce toxicity to osteoblasts [10]. Bulk BAG also presented better fracture toughness, hardness and bending strength when compared with commercial HAp bioceramic [11]. BAG has a monoclinic structure with the P21/c space group that is illustrated in the Appendices (Fig. A. 1) [12]. The synthetic BAG melts incongruently at approximately 1600 °C (1873 K) [13]. The methods of synthesizing BAG include sol-gel processing [14], high temperature solid-state reaction [15], solid-state sintering [12], and mechanical activation [16]. Together with a stable phase of $Ca_2ZrSi_4O_{12}$, BAG constitutes the stable ternary compounds of the CaO-ZrO_2-SiO_2 system with the following reactions from (1) to (5) at 800 °C (1073 K) or higher [17].

$$CaO + ZrO_2 = CaZrO_3 \quad (1)$$

$$2CaO + SiO_2 = Ca_2SiO_4 \quad (2)$$

$$ZrO_2 + SiO_2 = ZrSiO_4 \quad (3)$$

$$2Ca_2SiO_4 + CaZrO_3 = Ca_3ZrSi_2O_9 + 2CaO \quad (4)$$

$$2CaO + 3SiO_2 + ZrSiO_4 = Ca_2ZrSi_4O_{12} \quad (5)$$

The variety of compositions in the CaO-ZrO_2-SiO_2 phase diagram that were studied at approximately 1300 °C (1573 K) are presented in the Appendices (Fig. A. 2) [13]. It was observed that, at such temperature, phases of Ca_2SiO_4 and $CaZrO_3$ were in equilibrium with the BAG phase. Furthermore, Kwon et al. indicated that phases of ZrO_2, Ca_2SiO_4 and $Ca_3ZrSi_2O_9$ form at about 1604 °C (1877 K) from the liquid having composition of 0.166, 0.467 and 0.367 for ZrO_2, $CaCO_3$ and SiO_2, respectively (weight fractions, [18]). Note that the original publication stated the fractions to 5 decimal points accuracy.

Thermal spray methods are regarded as suitable techniques to deposit bioactive materials onto metallic surfaces. Among the available techniques, plasma spraying is the most commonly used for orthopedic devices and dental applications [19]. Compared to the conventional gas-stabilized systems, the water-stabilized plasma (WSP) process has several unparalleled parameters, such as high plasma jet enthalpy (approximately 10 times greater than commercial atmospheric plasma spray torches, APS), high plasma velocity, lower plasma density and a long jet, resulting in high process temperatures and allowing high feed rates [20, 21]. In addition, the WSP system provides a low cost of operation since water is the source of stabilization rather than costly gases [22] and the process is hence viable for the manufacturing environment. Key features of the advanced, hybrid WSP (WSP-H) technique are the ability of generating a high enthalpy plasma jet, a high velocity and low density plasma effluent, which are achieved by combining characteristics of a gas-stabilized plasma and the water vortex-stabilized plasma. The WSP-H is advantageous for high spray rates and high deposition efficiencies [23], which is a highlight of this research since it represents a comparative study to conventional APS.

In this study, BAG is employed as a bioactive coating for Ti6Al4V substrates using the WSP-H process. The WSP-H-produced BAG coating is presented as an alternative approach for current commercial hydroxyapatite APS coating. Details of phases and elemental analyses of the coatings are discussed, along with mechanical properties including hardness, elastic modulus, as well as wear and

scratch behaviors. Finally, the cell viability and osteogenic gene expression studies on the coated samples are presented to evaluate the bioactive properties of the WSP-H BAG after three days and seven days of cell culture.

2. Experimental and characterization procedures

2.1. Powder preparation and coating setup

Baghdadite powder was prepared at the University of Würzburg, Germany following the sintering method [24]. Initially, zirconium oxide (ZrO_2), calcium carbonate ($CaCO_3$) and silica (SiO_2) were mixed at a molar ratio of 1:3:2 for two hours. After that, the mixture was sintered for three hours at 1300 °C and then crushed into submicrometer sizes to obtain the BAG powders for subsequent consolidation processes. The submicrometer BAG powder could not be fed into the plasma system due to poor flow characteristics. To improve the flowability, BAG was agglomerated using 5 wt % polyvinyl alcohol (PVA, Sigma Aldrich, St. Louis, MO, USA)". The BAG powder was then manually crushed and finally sieved to the size range of 63 µm to 106 µm suitable for the WSP-H process. HAp powders with particle sizes between 45 µm and 125 µm were purchased from Medicoat (Etupes, France). Ti6Al4V of dimensions $20 \times 30 \times 2.5\ mm^3$ were used as substrates for the coatings. The substrates were grit blasted prior to deposition and cleaned in acetone in an ultrasonic bath to remove residual grit. For the respective coating depositions, two plasma spray torches were employed: a high enthalpy hybrid water-stabilized plasma torch (WSP-H500) developed at the Institute of Plasma Physics (Prague, Czech Republic) to produce the WSP-H coating, and a gas-stabilized plasma torch Metco 9MB (Oerlikon Metco, Westbury, NY, USA) to produce the APS coating.

Substrates in the WSP-H coating experiments were mounted onto a revolving carousel where the revolutions of the carousel with samples are adjusted to the torch vertical travel speed so that an even deposition of all samples is ensured (approximately 55 rpm). To prevent overheating, the process is interrupted after every six strokes of the torch, until the samples cool enough (a well-defined point as the temperature is measured in-situ by a thermo-camera and also a thermocouple connected to the rear

of one of the samples). To speed up the cooling, two air-blades are cooling the carousel: one of them is at the very back (i.e., at the position directly opposite to the torch) and one is at the side. As the air-blades runs constantly during the spraying, such arrangement also aids in preventing the samples heating to excessive temperatures, thereby helping to preserve the phase composition.

The WSP-H arc current was 500 A at a voltage of 300 V (i.e. power of 150 kW) with the plasma forming water consumption of 1L per hour, and the powder feed rate was 83 g/min. At the long stand-off distance of 370 mm, the robot movement in WSP-H spraying was set so that the relative travel speed was 30 mm/s. There was no pitch distance as a revolving carousel was used to hold the samples and the torch simply passed in an up-and-down manner (along 70 mm distance) in front of the carousel. The frequency of the carousel revolutions was optimized in many previous spray runs and studies so that an even coverage of the samples is ensured. With regards to APS, the current and voltage were set at 300 A and 70V, respectively. The APS torch travel speed was 150mm/s with the pitch of 6mm (50% overlap for each step), and the powder feed rate was 11 g/min. Table 1 presents the key setup parameters for the coating depositions.

Table 1. Plasma spray deposition parameters of the BAG WSP-H and HAp APS.

Coating	**Parameter**	**Value**
BAG *via* WSP-H	Stand-off distance (mm)	370
	Feeding distance (mm)	65
	Torch power (kW)	150
	Gas flow, Ar (slpm)	15
HAp *via* APS	Stand-off distance (mm)	90
	Primary gas flow, Ar (slpm)	30
	Secondary gas flow, H_2 (slpm)	5
	Powder carrier gas flow, Ar (slpm)	9
	Torch power (kW)	21

2.2. Coating characterizations

Phase composition of the powders and the two coatings were investigated using Bruker D8 Advance XRD system (Bruker AXS LLC, Madison, WI, USA) with Cu Kα radiation. The XRD system operated at 40 kV and 30 mA with a 0.05° step size and two seconds of dwell time to perform the scan of 2θ

angles from 20° to 70°. The Diffracplus EVA software (Bruker, Billerica, MA, USA) with the database PDF2018-PDF-2-Release 2018 RDB from the International Center for Diffraction Data (ICDD, Newtown Square, PA, USA) was used to index and analyze the phases.

Field emission scanning electron microscope Zeiss SUPRA™ 40VP (FE-SEM, Carl Zeiss AG, Oberkochen, Germany) with an incorporated energy dispersive X-ray Oxford INCA 250 detector (EDX, Oxford Instruments NanoAnalysis, Concord, MA, USA) operated at 5 kV and 20 kV was used to analyze the coatings' microstructure and elemental compositions, respectively.

Surface roughness of the coatings was measured by a surface roughness tester Surftest SJ-210 (Mitutoyo, USA) equipped with a stylus radius of 2.0 µm. Thirty readings were recorded for each coating to investigate their surface properties. This surface roughness tester measured the average surface roughness (R_a), root mean square deviation (R_q), and average of the five maximum heights (R_z) following the ISO 4287 standard [25]. The surface topography was also visualized using a 3D optical profiler system Veeco Wyko NT1100 (Bruker, Tucson, AZ, USA).

Porosity of the coatings was measured from their cross sections using an image analysis package developed in Matlab® (The MathWorks, Inc., Natick, MA, USA) based on the Otsu threshold method [26]. The high resolution images taken by light microscopy were converted into an 8-bit greyscale format with 256 gray scale levels and then converted to black and white images by applying the threshold level from the Otsu threshold method [27]. The porosity level was defined as the ratio of black pixels and total pixels in the black and white images. A minimum of 10 images were record and analyzed, with the average value taken.

The macroscopic hardness was studied by performing microhardness tests on cross sections of the coatings using Vickers microhardness tester (Micromet 2103, Buehler, IL, USA) at a load of 300 gf and dwell time of 15 seconds. Forty readings were recorded and Weibull method was used to analyze coating properties and reliability [28].

Local mechanical properties of the coatings with regards to deformation, hardness and elastic modulus were evaluated using nanoindentation (Hysitron TI Premier, Bruker, Minneapolis, MN, USA). Single nano-sized indents were performed (using a Berkovich diamond tip) at a load of 1000 μN to investigate the deformation behavior of the coating at different positions across the coating cross sections (2.5 μm gap between indents). The loading/unloading rate was constant at the rate of 200 μN/s (five seconds of loading, two seconds of peak-load holding and five seconds of unloading).The scanning probe microscopy (SPM) method visualized the surface by performing a pre-scan of the surface before the indentation, followed by a post-scanning the surface after the indentation to provide more information concerning surface deformation. Ten areas were selected, having a total of approximately 160 indents performed on each coating.

A high-speed indentation method, termed as extreme property mapping (XPM), in combination with the SPM technique, investigated the distribution of hardness and modulus across the coating cross sections. These tests were performed with areal footprints of 30 × 30 μm^2 across the coating with 400 indents in each location using a Berkovich diamond tip. Hardness and elastic modulus were calculated following the principle of Oliver and Pharr [29], where the elastic modulus in the calculation is termed as the reduced modulus; that is the combined modulus consisting of the indenting tip and the specimen. The applied load in the high-speed nanoindentation tests was 1000 μN, with the loading/unloading rate of 10000 μN/s, translating into 0.1 seconds loading time, 0.1 seconds holding time at peak load, and 0.1 seconds for unloading time. These results were depicted as property maps of hardness and elastic modulus of the tested regions. In order to have a better interpretation of the property maps, the indents should be close but not overlap each other. According to recent study by Phani and Oliver, the minimum indent spacing is advised to be about 10 times the penetration depth of the indents [30]. The indent spacing of 1.5 μm was selected for the XPM study. It is noteworthy that the trend of the reduced modulus generally follows the same trend as the elastic modulus of the specimen [29], so the measured value of the reduced elastic modulus can represent the elastic modulus of the coatings.

A cono-spherical 1 µm-diameter diamond tip was used for nano-scratch and nano-scanning wear tests. The nano-scratch tests were performed at a constant load of 1000 µN to traverse a 10 µm-scratch. Three scratches were performed in ten areas across the coatings. Similarly, at least ten tests were performed on areas at the cross sections to study nano-scanning wear. The wear studies were carried out by performing multiple scratches parallel to each other over the same location a constant load of 200 µN onto the area of $10 \times 10\ \mu m^2$ and scanned over the selected section three times for each location at a scan frequency of 0.8 Hz. The number of passes represents the number of full scans over the location and the step size was about 40 nm. The tip moved laterally along the scanned area with a step size such that each move will cut 40 nm into the sample at the force of 200 µN. The wear volume is calculated as the depth of penetration multiplied by the scan area. Note that these tests were performed under ambient atmospheric conditions with no *in vitro* environment. The nano-scratch test and nano-scanning wear test were performed on the coating cross sections. In the case of the scratch test, the scratch tracks were perpendicular to the coating-substrate interface to ensure that more splats could be scratched. In the scanning wear, the scan patterns were carried out parallel to the substrate interface, which can provide the collective wear behaviour of multiple splats.

2.3. Human osteoblasts (HOBs) seeding and viability test

Permission to use discarded human tissue was granted by the Sydney Children's Hospitals Network Human Research Ethics Committee and an informed consent was obtained. Human trabecular bone was used for isolating human osteoblasts (HOBs) as described previously [10]. The cells were cultured at 37 °C with 5% CO_2, and the culture medium (alpha-MEM (Gibco, USA) supplemented with 10% FCS, 100 units/ml Penicillin-Streptomycin (Gibco, USA) and 0.1mM L -Ascorbic acid 2-phosphate (Sigma, USA)) was changed every three days until the cells were passaged at 80-90% confluence. HOBs at passage 2 from three donors were pooled together and used for all experiments.

HOBs were first seeded on HAp and BAG coated coupons ($10 \times 10 \times 2.5\ mm^3$, cut from original coated samples) placed in a 24-well plate with a density of 3×10^4 cells/well in a 200 µl culture medium. The discs with seeded cells were transferred to incubator to allow cell attachment for 90 min, and then flooded with 500 µl culture medium and incubated for 3 or 7 days. HOBs cell viability on the discs was assessed using CellTiter 96® AQueous One Solution Reagent (Promega), which contains a tetrazolium compound [3-(4,5-dimethylthiazol-2-yl)-5-(3-arboxymethoxyphenyl)-2-(4-sulfophenyl)-2H-tetrazolium, inner salt; MTS] that is reduced by living cells to yield a colored water-soluble formazan dye. Briefly, 200 µL of MTS solution was added to each well and incubated for 4 hours at 37 °C under 5% CO_2, then 100 µL of the reacted reagent from each well was transferred to a 96-well plate to measure the absorbance using a microplate reader at a wavelength of 492 nm.

2.4. Osteogenic gene expression

HOB cells cultured in the previous steps were seeded onto surfaces of HA and BAG-coated discs and placed in a 24-well plate with a density of 3×10^4 cells/well in a 200 µl culture medium. Total RNAs were isolated from the cells seeded on the discs using RNeasy Kit according to the manufacturer's instructions (QIAGEN, Germany). Complementary DNA (cDNA) was then synthesized from 1.0 µg total RNA using SensiFAST cDNA Synthesis Kit from Bioline (Taunton, MA). Real-time polymerase chain reaction (PCR) was carried out using SensiFAST™ kits (Bioline (Taunton, MA) on Rotor-Gene 6000 (Corbett Life Science, NL). The relative mRNA expression levels of osteogenesis (RUNX-2), osteopontin, bone sialoprotein, and osteocalcin genes were obtained by normalizing to the house-keeping gene of 18S by using the previously used primers [10].

2.5. Statistical Analysis

All quantitative data presented in the manuscript is calculated as mean ± standard deviation (SD). The p-values of each data set (if presented) were calculated using a two-tailed unpaired t-test, where the statistical significance was defined as $p \leq 0.05$. Origin Pro 2018b (OriginLab Corporation, Northampton, MA, USA) was used to evaluate the statistical analysis.

3. Results and discussions

3.1. Phase compositions of coatings

Fig. 1 depicts the XRD pattern of the BAG powders and coating, while the XRD pattern of the HAp powders and coating is presented in Fig. 2. The peaks in the diffraction of BAG powders correspond to the crystalline phase of BAG (ICDD-PDF #00-054-0710). New peaks emerged from the BAG coating at approximately 31.8° and 32.2°. These peaks were indexed to the phase of larnite-Ca_2SiO_4 (ICCD-PDF # 00-033-0302) and is known to form from the quenching of molten $Ca_3ZrSi_2O_9$ [18]. On the other hand, the HAp XRD patterns were indexed with the phase of HAp (ICCD-PDF #00-064-0738) in both powders and the coating, and tricalcium phosphate-TCP ($Ca_3(PO_4)_2$) (ICDD-PDF #01-072-7587) in the coating..

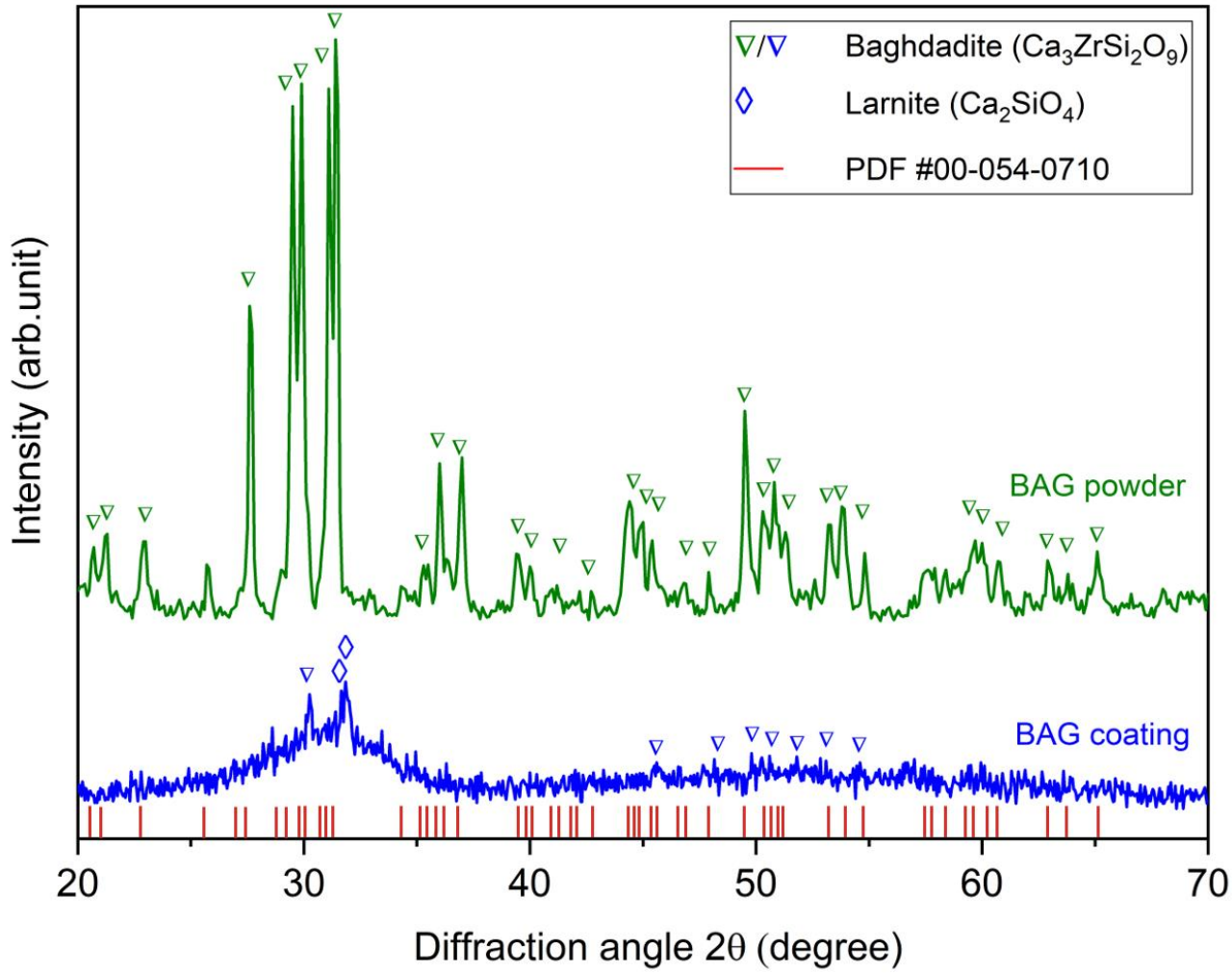

Fig. 1. XRD patterns of BAG powder and coating.

The method provided in the study of Sun et al. [31] was used to measure crystallinity from the XRD spectra. Both feedstock powders had high crystallinity (81.8% BAG, 86.8% HAp). Upon spraying, the crystallinity level of BAG WSP-H coating dropped to 22.9%, while the crystallinity of the HAp coating experienced a less significant reduction to ~72.8%. In other words, a large proportion of crystalline phases in the BAG coating has been transformed to amorphous phases. The crystalline level in a thermal spray coating depends on the melting behavior of the feedstock and the cooling rate. The formation of amorphous phases is a distinct feature of the plasma spray technique since the feedstock is melted in the high temperature plasma plume and then re-solidifies rapidly to form the coating [27]. The lower crystallinity of the BAG coating (i.e., greater amorphicity) arises from the more complex

structure of BAG since it belongs to the sorosilicate group [32]. A longer recrystallization time would be needed to accommodate the atomic ordering required to form this intricate structure. Furthermore, in the case of the BAG coating, compressed air was used to intensively cool the samples, so their temperature would drop faster. The re-solidification is extremely short and the molten particles are unable to recrystallize under equilibrium conditions; hence an amorphous phase forms.

The importance of the crystalline to amorphous phase proportion lies in their differing resorption rates *in vivo*. Amorphous phases resorb at a more rapid rate and hence their prominence controls the remodeling and stabilization of an orthopedic implant [31]. Amorphous phases promote bone in-growth during the early stage of implant insertion; consequently, the bone ingrowth produces better anchorage between the bone and implant [31]. However, these phases are not stable and lead to poor mechanical properties of the coating due to rapid dissolution and degradation [19]. Crystallinity, on the other hand, supports proliferation of bone cells and provides more stable mechanical properties that lengthens the lifetime of the implant [31]. In other words, a coating that possesses high crystallinity will exhibit a low dissolution rate. It is important to balance the level of crystalline and amorphous phases to achieve the joint outcomes of early bone cell attachment, cell proliferation and mechanical stability of the coating in long term. The amorphous phases can be transformed by heat treatment to the crystalline structure [19].

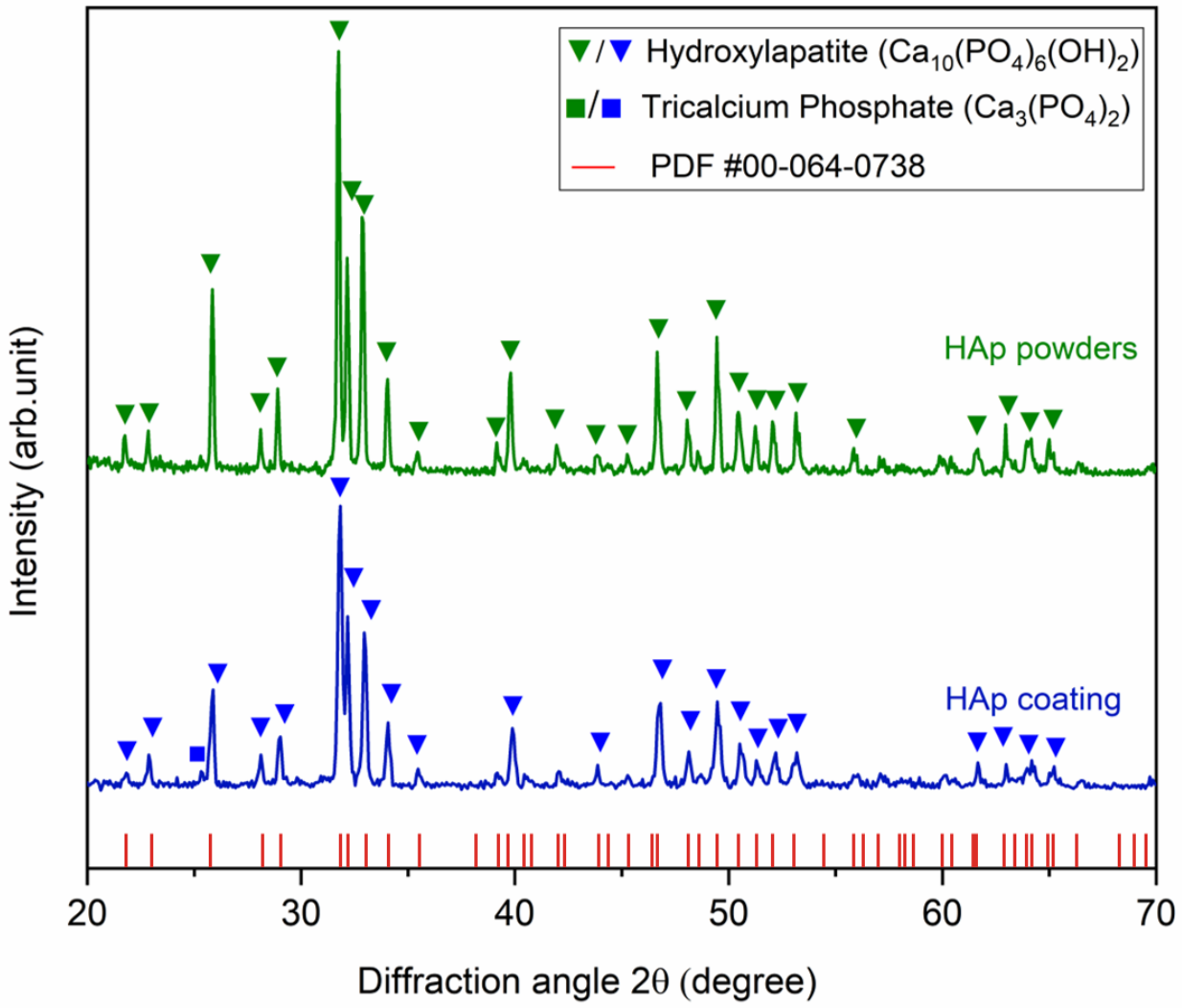

Fig. 2. Typical XRD patterns of HAp powder and coating.

3.2. Elemental compositions of coatings

Elemental distribution and representative elemental compositions at random locations of the BAG coating were assessed by area scanning and point EDX analyses, respectively (Fig. 3). The elements in the BAG coating are evenly distributed through the coating cross section as confirmed through the element maps in Fig. 3. EDX point analysis confirmed almost identical elemental composition at six randomly selected representative locations, Table 2. The calculated atomic Ca:Zr:Si ratios with an average of approximately 3:1:2 fit those of the pure BAG phase (3:1:2) in the CaO-SiO_2-ZrO_2 system [13]. Note that the other ternary phase $Ca_2ZrSi_4O_{12}$ having a ratio of 2:1:4 was not detected in the BAG coating [17]. This data confirms that the BAG phase was reformed in the coating upon plasma spray

deposition and presented as the major phase in the coating but in the form of glassy phase due to rapid quenching solidification process and remained in similar chemical composition to the starting powder. The Ca_2SiO_4 was present in the coating but did not reveal inconsistencies in the EDX maps. There were no visible inhomogeneities in the microstructure from Ca_2SiO_4 and is inferred that this phase existed in nanocrystalline form at a low proportion that was distributed throughout the BAG phase. The homogenous distribution of elements together with the uniformity of the BAG glassy phase and the larnite phase in the BAG coating (confirmed in the XRD result) are assumed to lead to consistent mechanical properties of the coating, which will be discussed in the following sections.

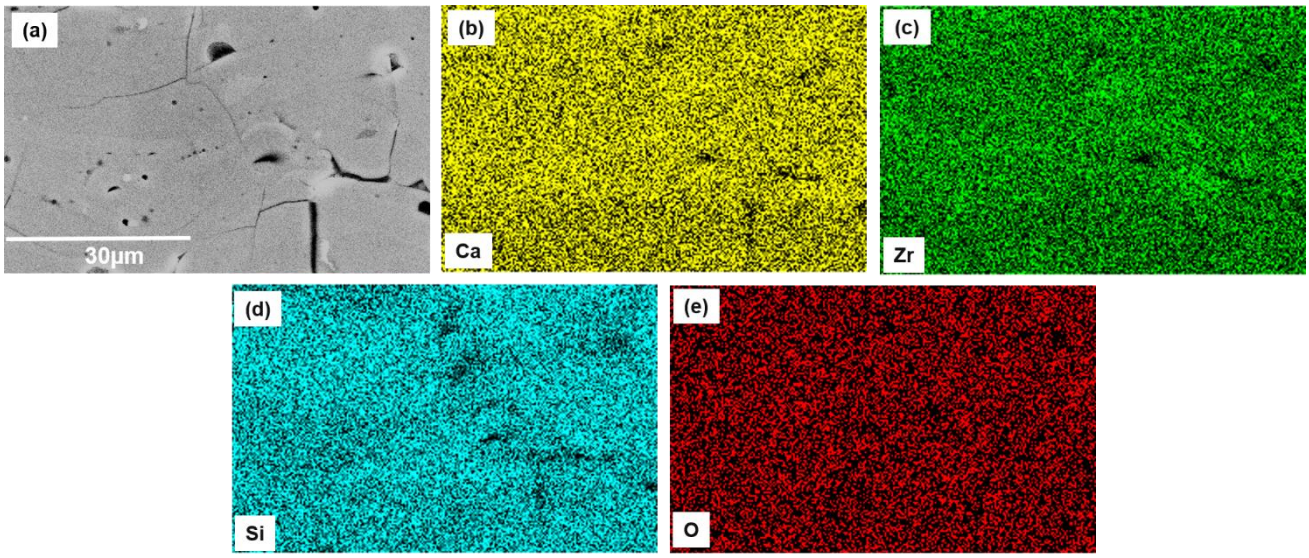

Fig. 3. EDX results of the BAG coating with maps of elemental distribution on arepresentative cross-section area.

Table 2. Elemental compositions of the BAG coating at six randomly selected locations, confirming the chemical homogeneity of the coating.

Position	**1**	**2**	**3**	**4**	**5**	**6**
Element	Atomic %					
Ca	19.8	19.1	19.9	19.1	20.0	19.6
Zr	6.3	6.1	6.4	6.9	6.1	7.0
Si	13.4	13.3	14.2	12.6	13.5	12.5
O	59.5	60.5	59.5	61.4	60.4	60.9
Ca:Zr:Si	3.1:1.0:2.1	3.1:1.0:2.1	3.1:1.0:2.2	2.8:1.0:1.8	3.2:1.0:2.2	2.8:1.0:1.8

The EDX results of the HAp coating depicted in Fig. 4 and Table 3 describe the elemental distributions and their representative atomic percentages at six locations across the HAp coating. The EDX maps depict the distribution of O, P, and Ca of the tested area presented in Fig. 4. Phases of HAp (Ca/P ratio ~ 1.67), TCP (Ca/P = 1.5) were detected in these locations, in accordance with the XRD results, while other detected Ca/P ratios suggest a formation of calcium-deficient HAp (1.5 < Ca/P < 1.67) and calcium-rich HAp (Ca/P > 1.67) phases [33]. In other words, despite the elemental distributions in Fig. 4 showing an even element distribution across the coating, the different EDX point analyses carried out at different locations may indicate a potential variation of mechanical properties, which will be further evaluated in the mechanical properties analysis.

Table 3. Elemental compositions of the HAp coating at six randomly selected locations, showing partial heterogeneity of the coating.

Position	**1**	**2**	**3**	**4**	**5**	**6**
Element	Atomic %					
O	65.3	61.1	61.8	65.3	67.9	69.2
Ca	20.9	24.3	13.5	21.4	19.6	19.5
P	13.8	14.6	24.7	13.3	12.5	11.3
Ca:P	1.51	1.66	1.83	1.60	1.55	1.73

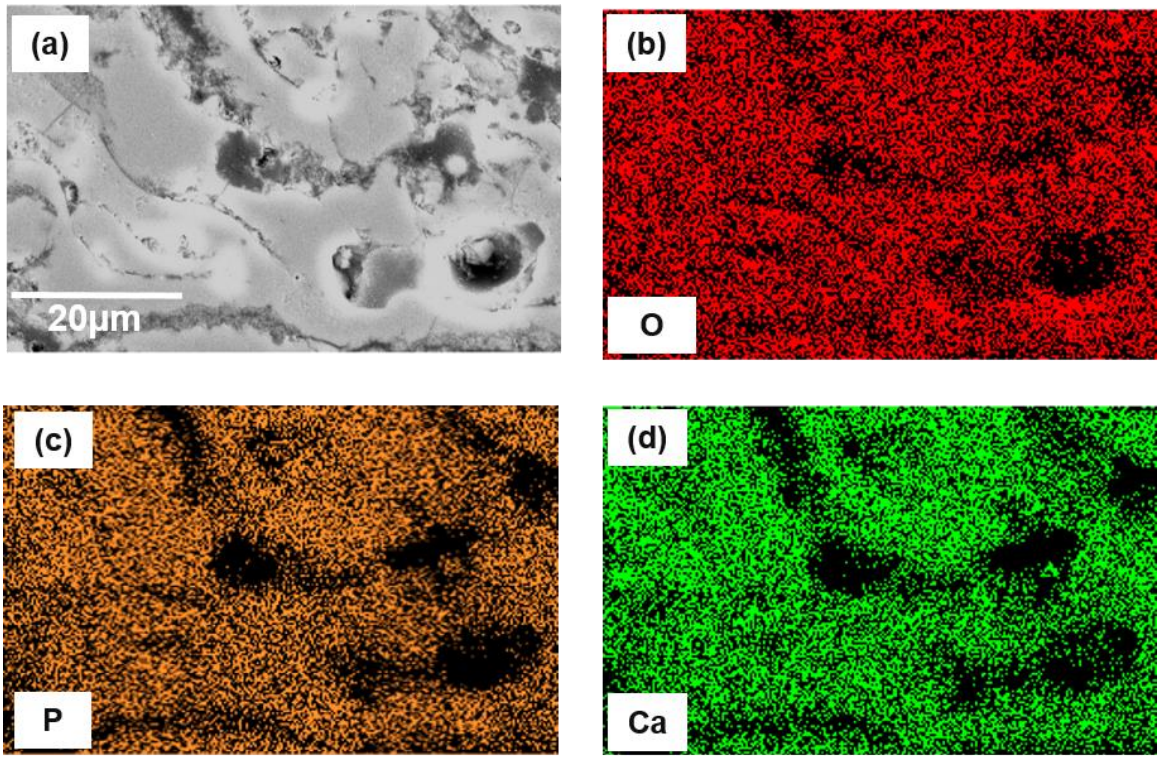

Fig. 4. Typical EDX results of the HAp with maps of elemental distribution on a representative cross-section area.

3.3. Surface profiles and surface roughness of coatings

The surface topography results of the BAG and HAp coatings are presented in Fig. 5; top views Fig. 5a and Fig. 5b), and surface roughness parameters (Fig. 5c) are shown. The different features observed on the 3D profiler maps (noise vs smooth) is due to the difference in surface features of the two coatings. The HAp coating with larger average particle size and the consistent sizes of the starting powder presented larger and consistent sizes of splats, while the BAG coating splats presented in smaller and various sizes. The results observed in the BAG surface were formed due to the breaking down of agglomerated powder into its initial sizes (submicrometer) during the plasma spray. As the result, the BAG surface shown more random texture with various sizes of splats that led to more noise and speckled features than the HAp surface. Both coatings have similar surface parameters with average surface roughness, R_a, for the BAG and HAp coatings reaching 9.67 ± 0.99 µm and

9.85 ± 0.83 µm, respectively. Additional surface roughness parameters are R_q = 12.12 ± 1.33 µm and 12.07 ± 1.01 µm, while R_z = 54.76 ± 6.46 µm and 53.63 ± 3.93 µm for the BAG and HAp coatings, respectively.

The surface roughness plays an important role in providing good interaction between the coating and the cell and can significantly influence the osseointegration process [19]. Indeed, our previous study indicated that such surface roughness values supported the attachment and proliferation of MG-63 osteoblast-like cells [34]. Thus, these results are, too, expected to promote cell attachment and growth of HOBs on the coating. Based on the above surface roughness parameters, it is observed that there is no difference (no statistical significance, $p > 0.05$) between the R_a roughness parameters of the BAG and HAp coatings. However, these amplitude parameters do not sufficiently explain the different surface textures presented in Fig. 5a and Fig. 5b.

More information of the surface texture derives from a hybrid parameter known as the developed interfacial area ratio (Sdr), which is also termed as the 'surface complexity'. The Sdr results of the two surfaces are significantly different, Sdr BAG = 1240.0 ± 56.8 % and Sdr HAp = 386.3 ± 13.4 % (n = 10); while Sdr of the grit blasted substrate is 64.0 ± 3.4 %. Hence, the random texture with more noise and speckled features can be confirmed through the higher result of surface complexity (Sdr) for the BAG coating in comparison to the HAp coating.

The higher Sdr value in the BAG coating indicates that the BAG surface provides more surface area (illustrated in Fig. A. 3) to support cell attachment. In short, although the amplitude parameters of the surfaces are similar, the differences in the developed interfacial area ratio as well as surface chemistry between the two coatings could induce different behaviors in cell attachment and proliferation. .

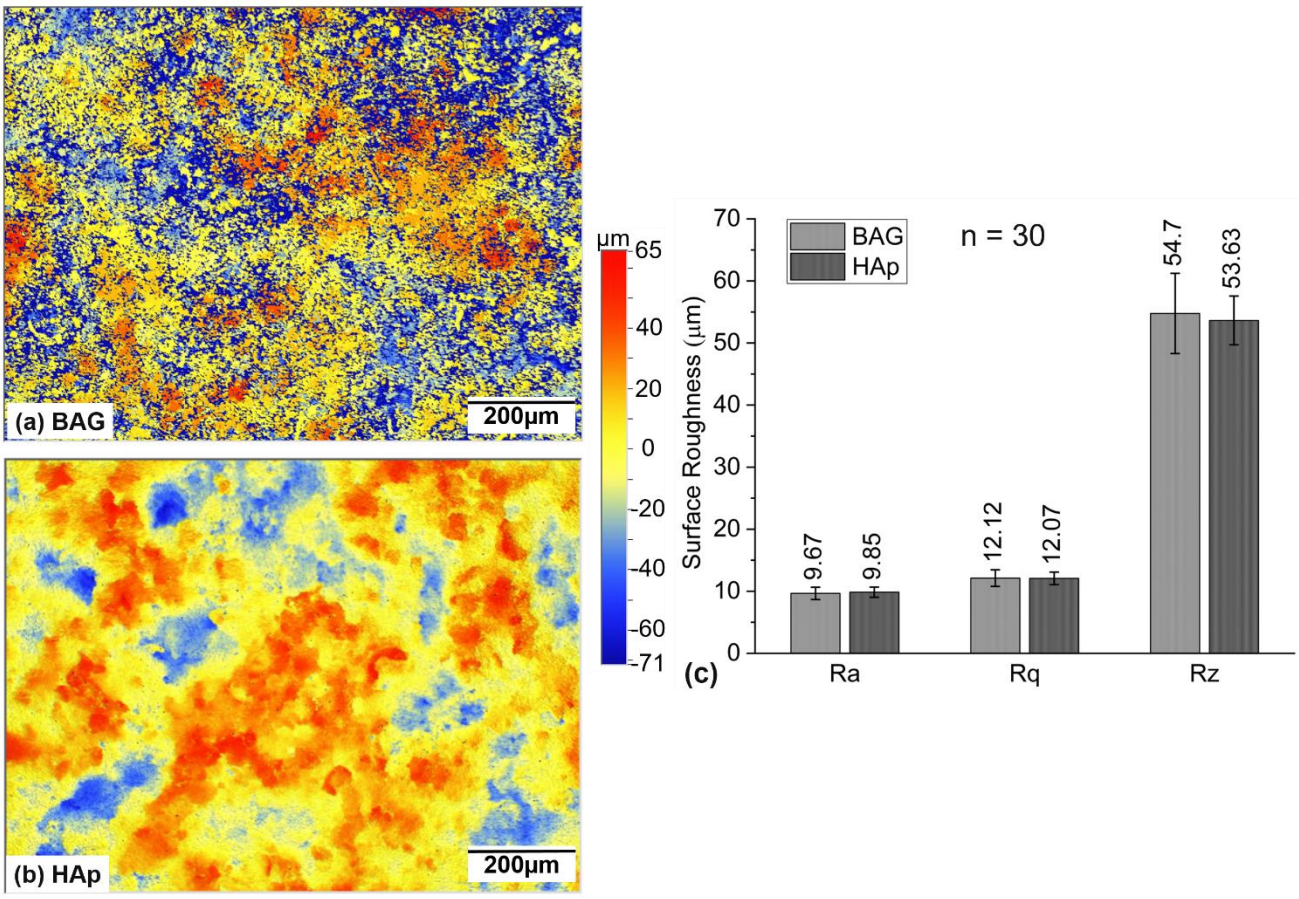

Fig. 5. Typical surface topography profile: (a) the BAG WSP-H coatings; (b) the HAp coating; and (c) surface roughness parameters of the coatings.

3.4. Coating microstructures

Microstructures of the BAG and the HAp coatings are shown in Fig. 6a and Fig. 6b, respectively. It is evident that the BAG coating possessed a more uniform microstructure, with less cracks and a good interfacial contact between the coating and the Ti6Al4V substrate without signs of coating delamination. On the other hand, morphological features in the HAp coating show different contrasts between amorphous and crystalline areas. The amorphous areas are preferentially removed during the polishing process and exhibit a darker contrast, a phenomenon intensively studied in HAp coatings by Gross et al. [35, 36]. Some cracks can be observed at the interface between the coating and the substrate for the HAp coating that could potentially deteriorate the mutual bonding strength.

The pores within the BAG coating range from 5 µm to 10 µm and the porosity level is 6.98 ± 1.23% (n = 12). The HAp coating exhibited a slightly higher porosity of 9.29 ± 1.20% with a pore size distribution from 5 µm to 12 µm. In general, the porosity for a commercial HAp coatings ranges from 3% to 20% [37], i.e., both coatings investigated in this work fall within this range. Porosity is a preferable characteristic of bio-coatings for orthopedic implants. Porous structures can promote an osteophilic surface for the penetration and attachment of bone cells. A coating with porous structure can also enhance implant fixation due to the ingrowth of tissue into the pores [31]. Porosity also supports more rapid dissolution behavior that can stimulate bone growth. At the same time, care must be taken concerning the porosity level, since pores, especially at the interface of the coating/substrate, detrimentally influence the bond strength of the coating as well as the cohesive strength among splats [38]. A high proportion of porosity can also diminish the coating strength, leading to crack growth and even coating delamination [31]. Hence, it is important to balance the porosity level in the produced coatings for orthopedic implants to support osteointegration, while maintain mechanical properties of the coatings.

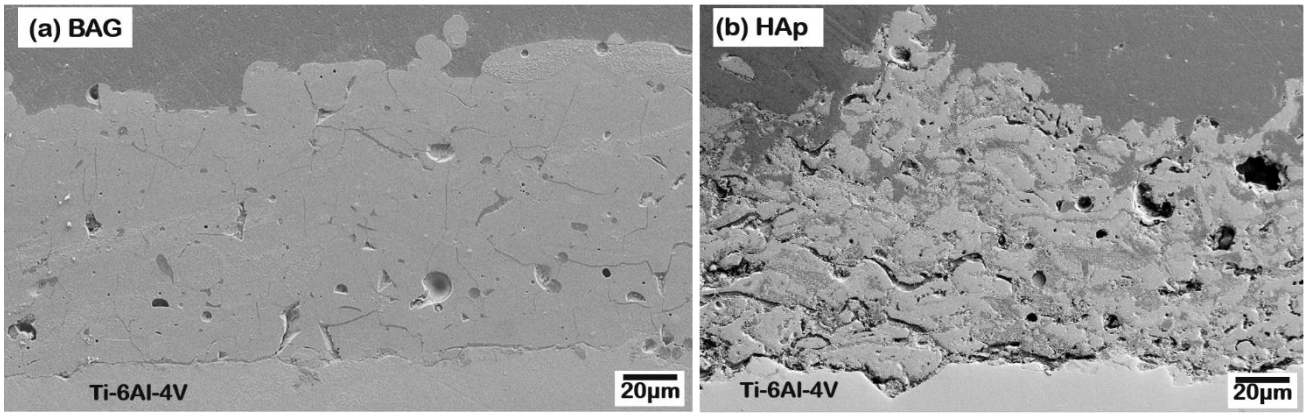

Fig. 6. Microstructure of (a) BAG WSP-H and (b) HAp APS coatings.

3.5. Vickers microhardness

The Vickers microhardness of the BAG coating was notably higher than that of the HAp coating (statistical significance $p < 0.05$), with the average values of 345.1 ± 36.8 $HV_{0.3}$ vs. 114.7 ± 19.0 $HV_{0.3}$ for the BAG and the HAp coatings, respectively. The higher hardness of the former arises from the

inherent feature as a Ca-Si bioceramic and the incorporation of zirconium into this Ca-Si bioceramic. BAG is a sorosilicate ceramic that has $[Si_2O_7]^{6-}$ as the base chemical group formed from two silicate tetrahedrons linked by one oxygen, and Zr^{4+} from ZrO_6 octahedral [15]. As the result, the $[Si_2O_7]^{6-}$ and ZrO_6 can create a strong network that enhance the stability of the BAG structure [39]. This result is in accordance with our previous study [34]. Similarly, Schumacher et al. demonstrated that the BAG bulk ceramic possess higher fracture toughness and hardness than that of the HAp bulk ceramic [11].

One of the common approaches for statistical analysis of mechanical properties, especially microhardness of thermally sprayed coatings, is the Weibull method, which describes the lifetime problems and mechanical properties of brittle materials [40]. The Weibull analysis is typically represented by the scatter in data (i.e., the Weibull modulus, *m*) together with the support of the goodness of fit (R^2) as the non-linear least squares fit procedure. A higher Weibull modulus *m* demonstrates less variation in the results, while the higher R^2 value indicates the Weibull distribution parameters fit better to the available data. [40, 41].

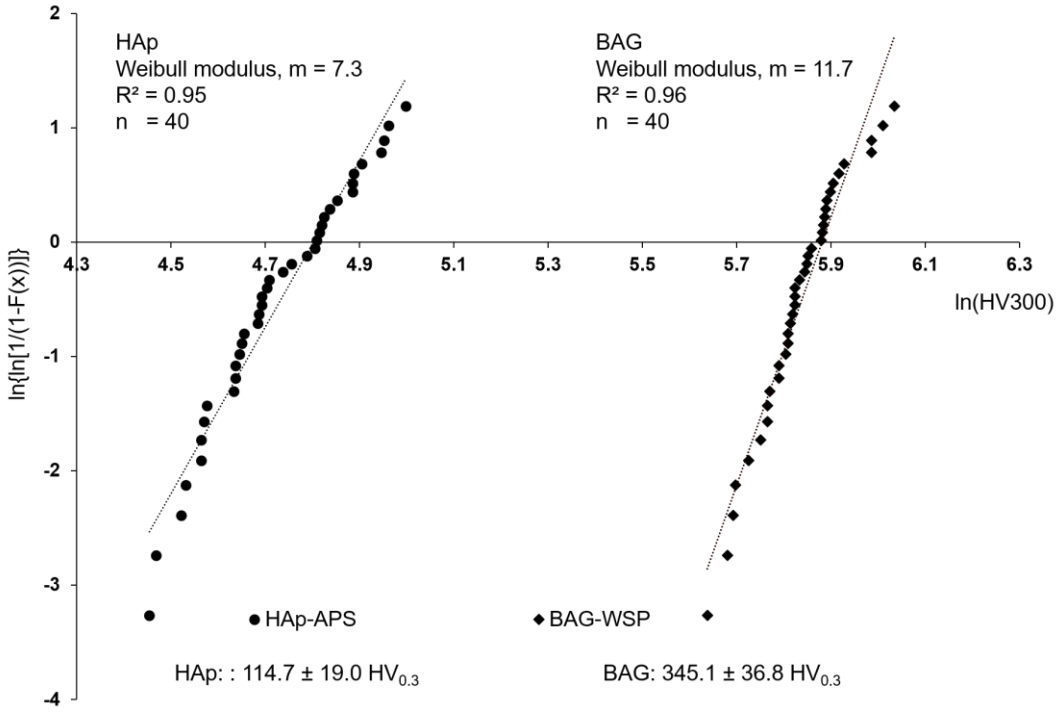

Fig. 7. Weibull analysis of Vickers hardness results of BAG and HAp coatings.

The Weibull analysis presents curve fitting with good regression fits R^2 values of 0.95 and 0.96 for the HAp and the BAG coatings, respectively (Fig. 7). The higher Weibull modulus *m* of the BAG coating (*m* = 11.2) than that of the HAp coating (*m* = 7.3) implies lower variation in the hardness for the BAG coating; this is, again, in accordance with the more homogeneous structure of the BAG coatings presented in Fig. 6.

3.6. Nanoindentation

Fig. 8a and Fig. 8b illustrate selected regions in the cross section of the BAG coating prior to and after the nanoindentation, respectively. The rather identical indent sizes in Fig. 8b are consistent with the depths of penetration of the corresponding series 1, 2, 3 and 4 presented in Fig. 8c, where the arrows indicate the position of the individual indents. The average penetration depth in the BAG coating was approximately 20 nm (Fig. 8c).

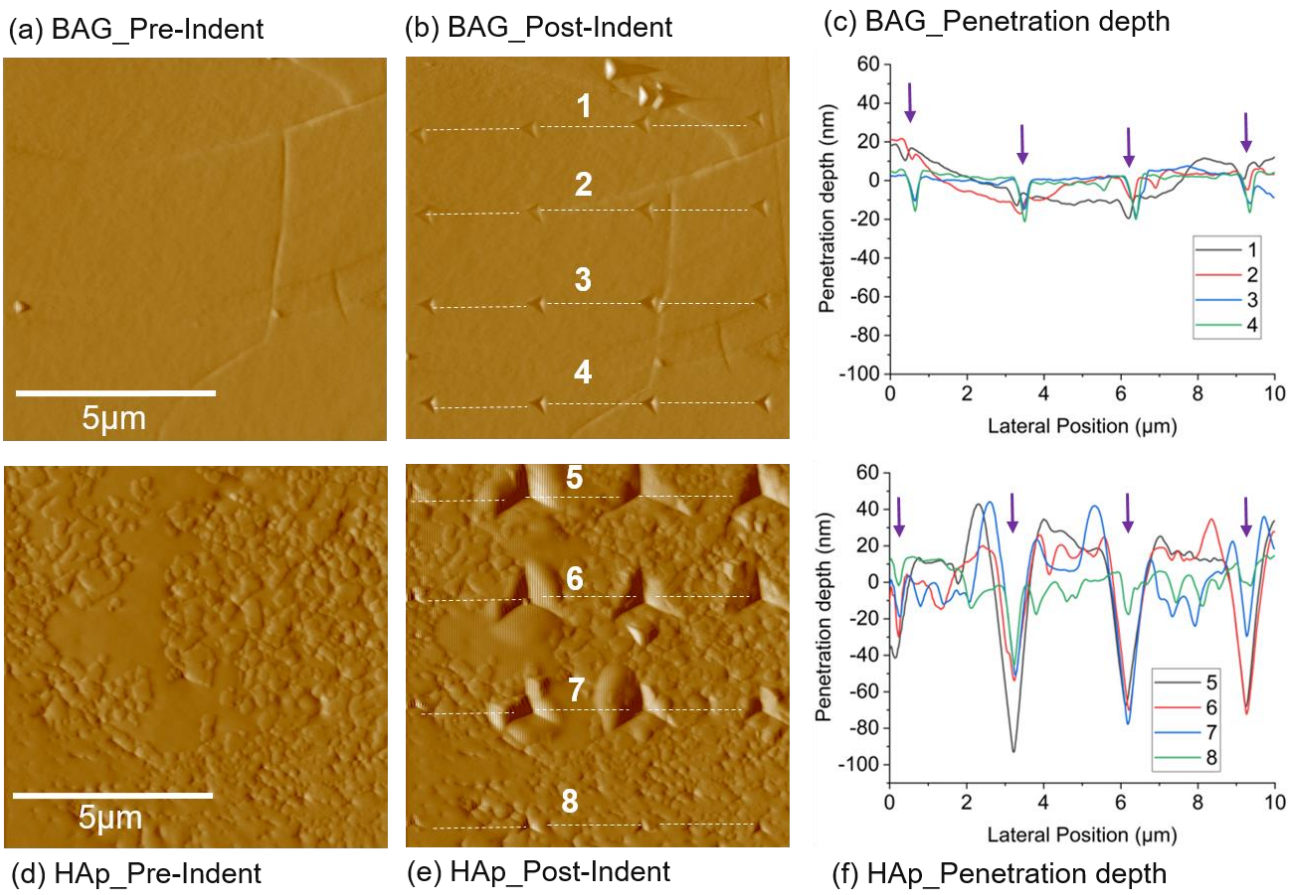

Fig. 8. Nano-indentation of the BAG coating (top) and the HAp coating (bottom). (a) and (d) SPM images before the indentation, (b) and (e) SPM images after the indentation, (c) depth of penetration of indents series 1, 2, 3, 4 from (b), (f) depth of penetration of indents series 5, 6, 7, 8 from (e). The arrows indicate the positions of indents, indent spacing: 2.5 μm.

The indentation results for the HAp coating show greater variance in the indent sizes (Fig. 8e), reflected in the larger range of penetrated depths in Fig. 8f, with the indent depths of the HAp coating ranging from 20 nm to 100 nm (Fig. 8f). These depths are compatible with the minimum indent spacing requirement [30]. This result indicates that, even at micro-scale level, the BAG coating exhibits a more uniform mechanical properties (hardness) compared to the HAp coating. In fact, the consistency in the sizes and penetrated depths of the indents in the BAG coating suggest that this coating is more reliable than the HAp coating.

A higher density of indents (400 indents on a $30 \times 30\ \mu m^2$ section) was executed to study the distributions of hardness and elastic modulus of the coatings by using the XPM technique (Fig. 9). There are similarities to the results of the single indent analysis. The hardness and elastic modulus of the BAG coating exhibit uniform distributions across the cross section (Fig. 9d and Fig. 9e). In addition, at the Zr-rich area (denoted by white arrow in Fig. 9 and shown in more detail in Fig. 10), higher values of hardness and elastic modulus were measured.

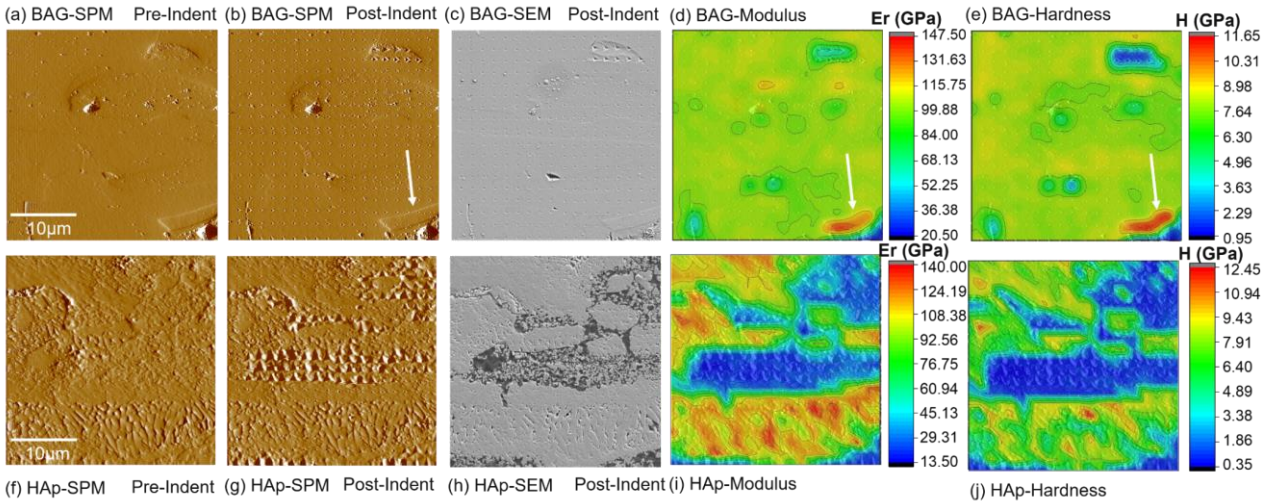

Fig. 9. Distributions of hardness and elastic modulus of the BAG coating (top) and the HAp coating (bottom): (a) and (f) SPM images before indentation; (b) and (g) SPM images after indentation; (c) and (h) SEM images at indented regions, darker areas are amorphous and lighter areas are crystalline areas in HAp; (d) and (i) distribution of elastic modulus; (e) and (j) distribution of hardness (indent

spacing: 1.5 µm).

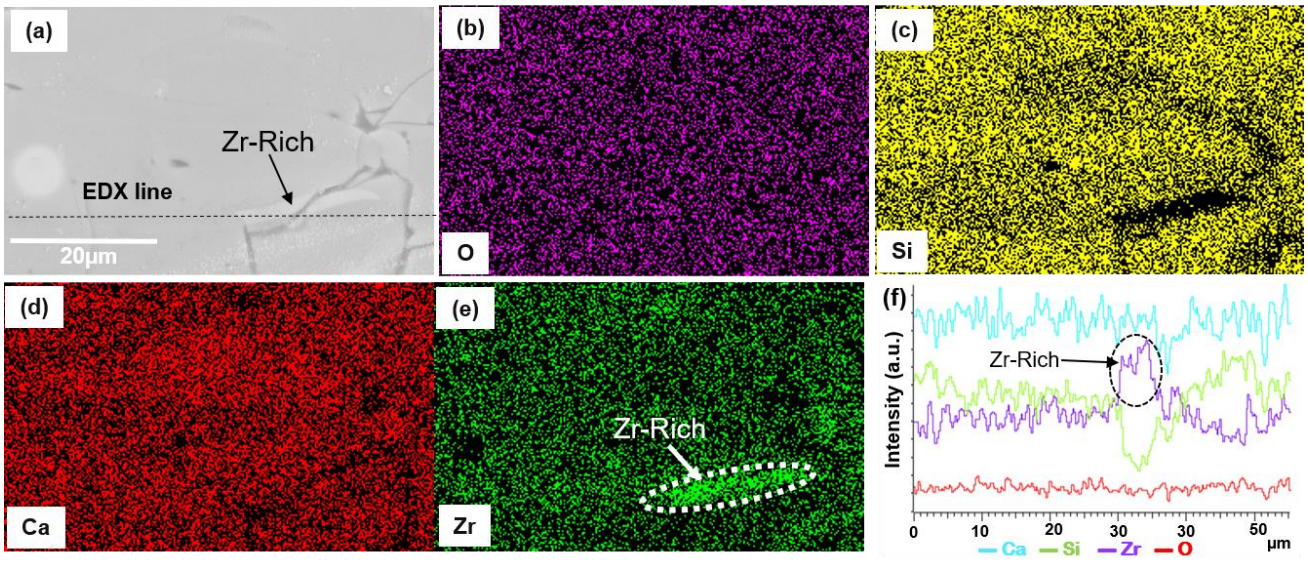

Fig. 10. Localized EDX mapping of the BAG coating. The highlighted area indicates a Zr-rich region.

In contrast to the uniformity of the BAG coating, the HAp coating shows wider deviations in the indent sizes as well as penetration depths (Fig. 9g). These fluctuations are reflected in the high variance in hardness and elastic modulus as indicated by significant color changes in Fig. 9i and Fig. 9j. In general, the lower values of hardness and elastic modulus correspond to areas consisting of the amorphous phase. The amorphous areas in the HAp coating are more vivid in the SEM image in Fig. 9h, distinguished by its darker contrast, in line with the studies of Gross et al. [35] [36], and also as confirmed in our previous study [42]. The average hardness and elastic modulus of the BAG coating were 7.75 ± 1.37 GPa and 101.94 ± 12.37 GPa, respectively, while the corresponding values for HAp were 4.45 ± 3.54 GPa and 63.97 ± 38.79 GPa. In general, the BAG coating therefore exhibited greater hardness and elastic modulus properties with lower variance than those in the HAp coating (statistical significance $p < 0.05$).

3.7. Nano-scratch

Nano-scratch tests and scanning wear tests were performed to address the splat-to-splat cohesion that is related to micromotion. Micromotion can cause splat fracture that leads to fragmentation and a poor

clinical outcome of osteolysis [43]. The nano-scratch results in the BAG coating reveal trends that are similar to the uniform distribution of hardness and elastic modulus. The uniform wear artifacts and penetration depths at three different scratched locations of the BAG coating are depicted as the SPM image in Fig. 11a. The average penetration depth for the BAG coating is 46.3 ± 15.7 nm with a coefficient of variance (CoV, standard deviation/mean) of 34.0%. The depth profiles of the scratch 1, 2 and 3 along the scratch direction on the BAG coating are presented in Fig. 11c that indicate the uniformity in scratch resistant ability of the BAG coating. In addition, the coefficient of friction (CoF) of the BAG also presents uniformly among these three scratch lines with the average value of 0.15 ± 0.02 and CoV of 13.0% (Fig. 11d).

In contrast, the scratches in the HAp coating behave significantly different along the scratch length presented in Fig. 11e, which could derive from the difference in behavior between the amorphous regions and crystalline regions as mentioned in the section 3.6. These differences are highlighted in the topography of the HAp coating in Fig. 11f, where significant changes in colors can be seen along these scratches. It is noteworthy that the range of the lowest and highest points in the HAp surface (from -133.0 nm to 133.0 nm) is much more than that of the BAG surface (from -16.7 nm to 16.7 nm).

The HAp scratches experienced plastic deformation at the second half of the scratch length with larger pileup can be seen in Fig. 11e & Fig. 11f. As the result, significant increase in CoF values could be seen in the dotted ellipses in Fig. 11h due to the increasing in the lateral force. The accumulation of deformed material in these regions will strongly affect the CoF values that does not actually represent the true values of CoF in these areas. Hence, the evaluation in CoF results of the HAp coating will not consider these regions. In fact, the deviations in depths of penetration of the HAp coating shown high variation in Fig. 11g, giving rise to a high data scatter; the average depth was calculated as 181.3 ± 164.7 nm with CoV 90.1%. The friction coefficients of the HAp coating suffered from the heterogeneity as well, varying from 0.04 to 0.37 and having an average of 0.32 ± 0.21 with

CoV of 65.3%. The inconsistent results are easier to understand by observing the detailed depth profiles at different locations (line 4, 5, and 6 in Fig. 11e) and the CoF results (Fig. 11h).

In short, both depth of penetration and CoF analyses showed remarkably better results for the BAG coating than those of the HAp coating ($p < 0.05$), where the BAG coating displayed better scratch resistance than the HAp coating.

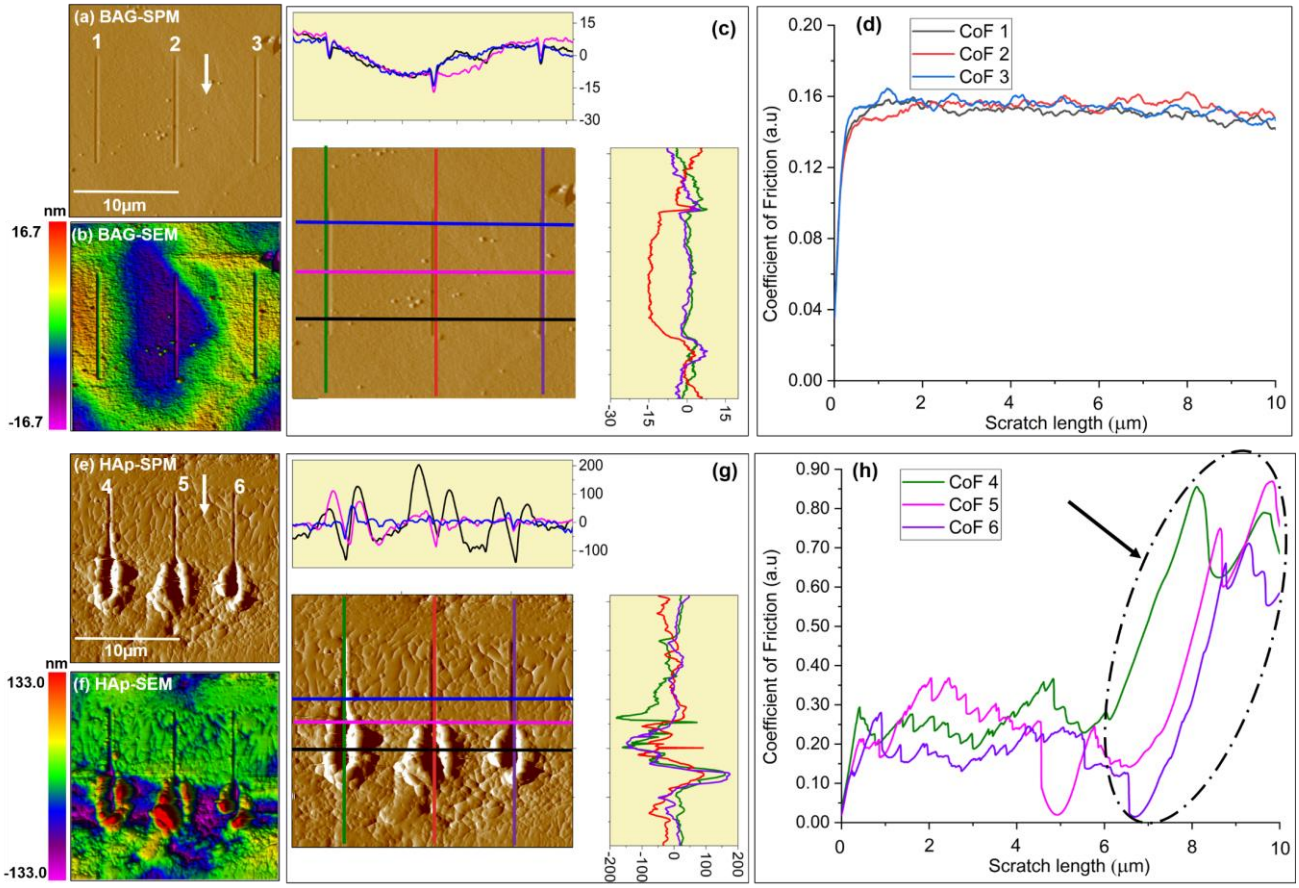

Fig. 11. Nano-scratch results of the BAG coating (top) and the HAp coating (bottom). (a) and (e) SPM images of the scratches, (b) and (f) surface topography of the scratches, (c) and (g) respective profiles at the indicated locations, (d) and (h) friction coefficients results. Dotted ellipse present ploughed locations along the scratches on the HAp coating. The white arrows indicate the direction of the scratching.

3.8. Nano-scanning wear

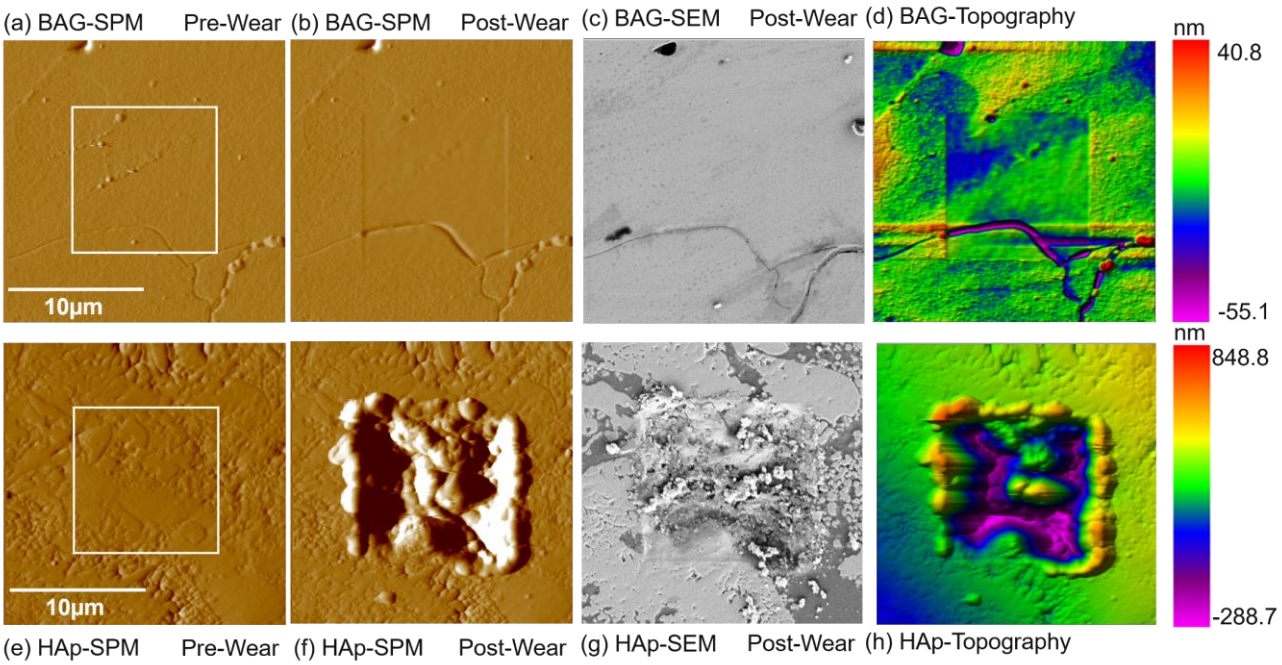

Fig. 12. Nano-scanning wear results of the BAG coating (top) and the HAp coating (bottom). (a) and (e) SPM images before wear test; (b) and (f) SPM images after wear test; (c) and (g) SEM images after wear test, (d) and (h) topography of the wear tested regions. The white squares indicate the tested areas.

Representative sections of the scanning wear tests for each coating are presented in Fig. 12, where the top and bottom rows present the result of the BAG and HAp coatings, respectively. The results of the BAG coating present a more consistent behaviour with low wear volume, as indicated by low and uniform material removal in the white square region in the top row of Fig. 12. In contrast, the results of the nano-scanning wear test in the HAp coating reveal uneven and, more importantly, a higher amount of volume removal in the bottom row. The unevenness may again stem from the presence of the crystalline and amorphous phases presented in darker and lighter regions, respectively. The values of wear volume are 0.16 ± 0.06 μm^3 and 5.52 ± 2.90 μm^3 for the BAG coating and the HAp coating, respectively. The BAG coating therefore presented significantly lower wear volume (~3% of HAp), with lower variance among the tested locations in comparison to the HAp coating. As presented in the hardness evaluation, the BAG coating possesses remarkably higher hardness than the HAp coating.

Furthermore, the BAG coating formed as a single-phase coating, yielding a consistent distribution of hardness. Both factors triggered the more consistent wear resistance behavior of the BAG coating and its overall better performance in comparison with the HAp coating.

Typical profiles of the coating surface after performing the nano-scanning wear tests are presented in Fig. 13 to provide further information on the wear depths. Lower depths and more consistent results are shown in the BAG coating, while high variances can be found for the HAp coating. These results are in agreement with the previous mechanical testing results and, yet again, demonstrate that the BAG coating presents consistent behavior. Importantly, the nano-scanning wear test has shown that the BAG coating possesses a better wear resistance than its HAp counterpart.

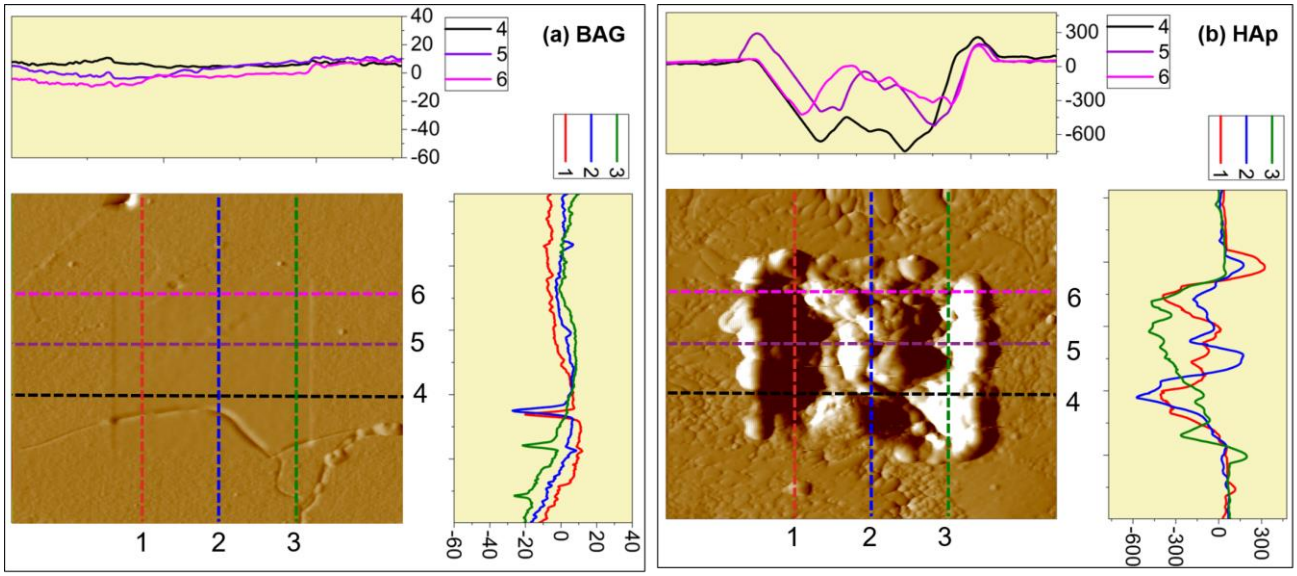

Fig. 13. Typical surface profiles after performing the nano-scanning wear tests on (a) the BAG coating and (b) the HAp coating.

3.9. HOBs viability test

Baghdadite, being a Ca-Si-based bioceramic, is expected to demonstrate improved bioactive properties *in vitro* compared to traditional calcium phosphate bioceramics [44]. The results of HOBs that were cultured on both HAp and BAG-coated surfaces with regards to the attachment and proliferation after 3 days and 7 days are presented in Fig. 14. At the 3rd day of incubation, the absorbance for the BAG

coating at the wavelength of 492 nm was 37.9% ± 3.1%, which was higher than the HAp coating that indicated an absorbance of 25.2% ± 4.1%. This result shows that both coatings possessed good biocompatibility in supporting the initial attachment of HOBs, with the BAG coating exhibiting a higher level of HOBs attachment.

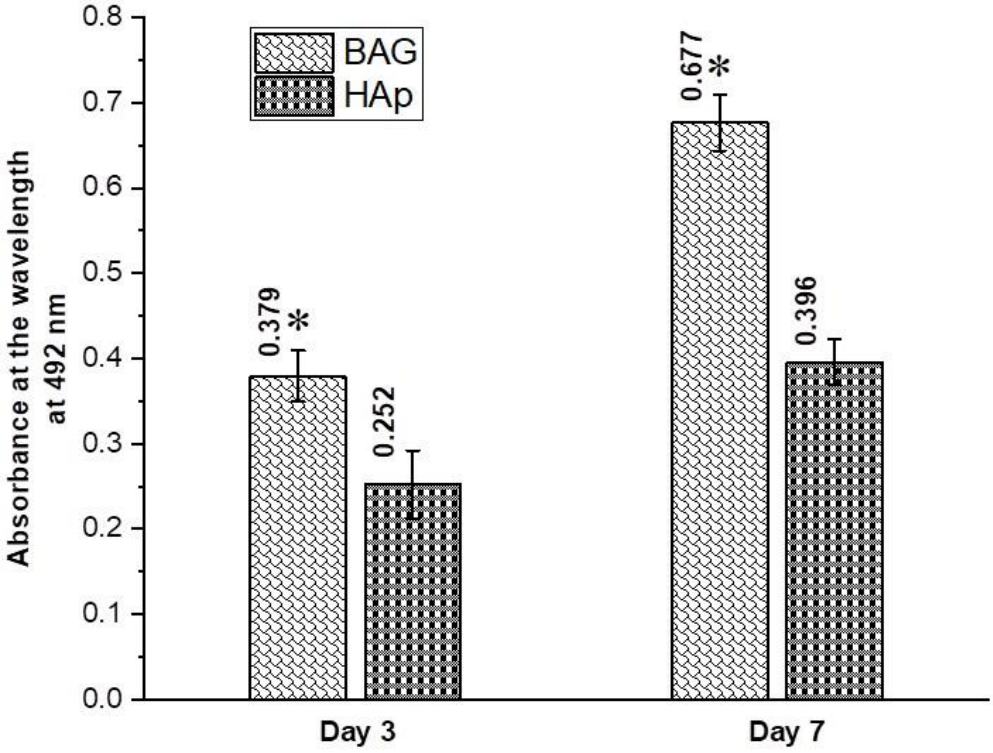

Fig. 14. HOBs viability test on BAG and HAp coatings (n = 5, duplicated tests, *: statistically significant, $p < 0.05$).

After 7 days of incubation, the absorbance rate of HOBs for BAG was increased significantly to 67.7% ± 3.4%; whereas the HAp coating revealed a smaller increase with an absorbance rate of 39.6% ± 2.7%. The previous discussion has shown that BAG and HAp coatings presented similar amplitude parameters of surface texture, but the BAG coating possesses higher surface area than the HAp coating that is indicated by the greater surface complexity (Sdr). The BAG coating would promote more cell attachment initially and stimulate cell proliferation in later stages. In addition, the surface coating chemistry will also play an important role in supporting cell attachment and proliferation. Baghdadite, in its bulk form, possesses bioactive properties that can trigger osteogenesis,

increase osteoblast cell proliferation and alkaline phosphatase (ALP) activity [10]. The observed improvement of BAG could result from the inherent characteristic of Ca-Si based bioceramic as well as changes in ion dissolution comparing with the HAp as a Ca-P based bioceramic [14]. These distinct properties are expected to be conferred to the BAG coating and support the attachment and proliferation of HOBs. As a result, the higher proliferation rate in the BAG was induced by an ability to support the attachment and proliferation of HOBs due to its Ca-Si-based bioceramic character. In short, compared to those cells on the HAp-coated surface, significantly more viable HOBs are present on the BAG surface at both the 3^{rd} and 7^{th} day that indicates the BAG coating is more favorable for HOBs adherence and growth than the HAp coating.

3.10. Osteogenic gene expression

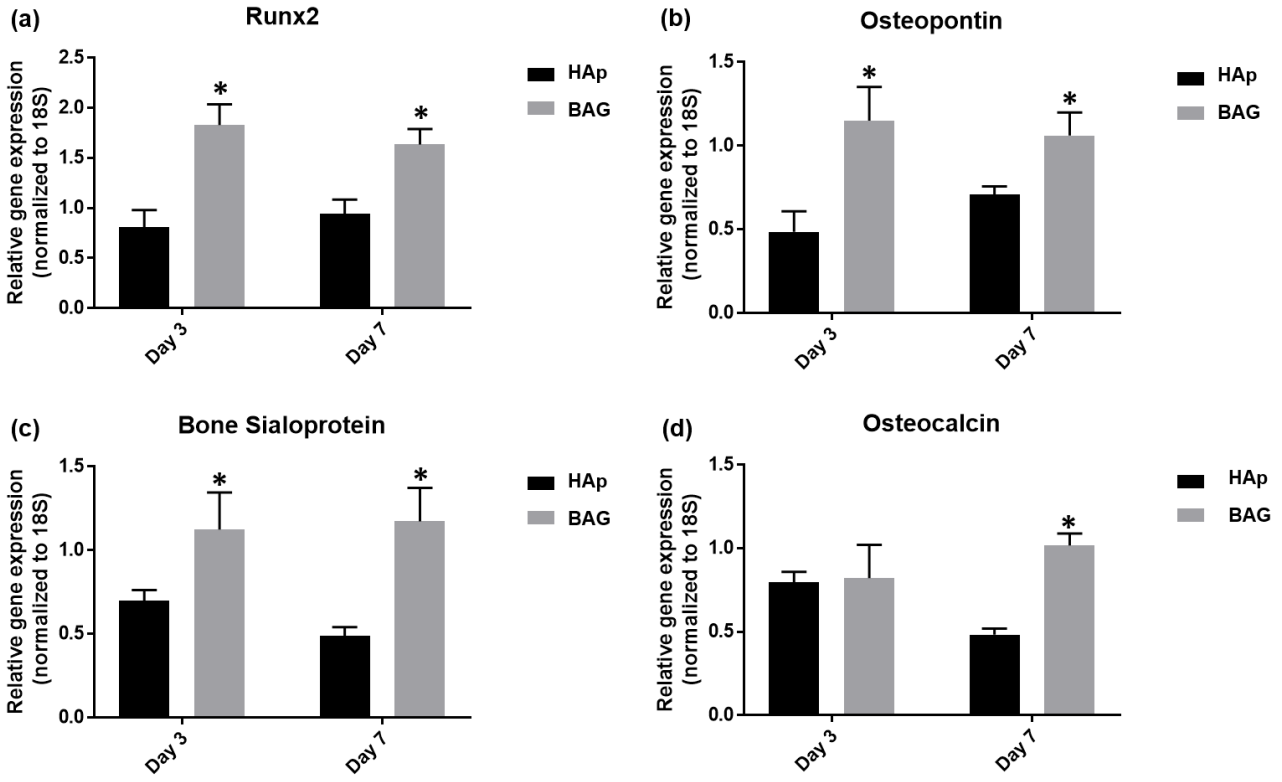

Fig. 15. Real time PCR analysis of the expression of different HOB markers (a) *RUNX2*, (b) osteopontin, (c) bone sialoprotein, and (d) osteocalcin on the surface of HAp and BAG coatings after three and seven days of culture, (n = 5, duplicated tests, * $p < 0.05$).

Real-time PCR results indicate the effects of the BAG and HAp coatings on osteogenic gene expression in HOBs after seeding and culturing HOBs for 3 and 7 days (Fig. 15). The relative gene expression of *RUNX2* on BAG and HAp samples after 3 days are 1.8 ± 0.4 and 0.8 ± 0.3, respectively, while after 7 days, the results are 1.6 ± 0.3 and 0.9 ± 0.3 (Fig. 15a). Similarly, osteopontin expression also shows results for the BAG and HAp samples after 3 days and 7 days ($p < 0.05$): 1.2 ± 0.4 and 0.5 ± 0.2 after 3 days and 1.0 ± 0.3 and 0.7 ± 0.1 after 7 days, respectively (Fig. 15b). Interestingly, the trends differed for the two coatings: the BAG samples exhibited a slight decrease from the 3rd day to the 7th day, whereas the HAp samples showed a converse increasing trend but the overall result of HAp is still lower than that of the BAG result. In short, both *RUNX2* and osteopontin presented a significantly higher gene expression (at $p < 0.05$) for BAG than for HAp-coated samples at both the 3rd and 7th day.

These trends of gene expression were similar for bone sialoprotein and osteocalcin (Fig. 15c and Fig. 15d), in that the data for BAG was significantly higher (at $p < 0.05$) than for HAp at both time intervals. However, the trends with regard to time were directly opposite to those of RUNX2 and osteopontin: the BAG tended to increase, whereas the HAp decreased. Quantitatively, the bone sialoprotein expression levels of BAG were 1.1 ± 0.4 and 1.2 ± 0.4 after 3 days and 7 days, respectively, while the HAp samples presented levels of 0.7 ± 0.3 and 0.5 ± 0.1 after 3 days and 7 days, respectively. In the case of osteocalcin, there was no difference in the expression level after 3 days between samples of BAG and HAp coatings at 0.8 ± 0.4 and 0.8 ± 0.2. However, this changed after 7 days, where, in the case of BAG the value increased to 1.0 ± 0.1, while it dropped for HAp to 0.5 ± 0.1, yielding the two values statistically different (at $p < 0.05$).

In all cases, the HOBs cultured on a BAG-coated surface showed significantly higher gene expression levels for *RUNX2*, osteopontin, bone sialoprotein, and osteocalcin, compared with those on HAp-coated surfaces after 3 and 7 days of culturing (at $p < 0.05$). This result for coatings agrees with results of other researchers where Ramaswamy *et al.* [14] have found that bulk BAG presents significant improvement in the capability of gene expression. The mechanism of improving the gene expression level in BAG samples could derive from the release of Ca and Si ions into the culture medium that stimulates the differentiation of HOBs [14]. The higher results of gene expression in the BAG coating indicates that the BAG coating is more favorable in supporting the differentiation of HOBs than the HAp coating.

4. Concluding remarks

The hybrid water-stabilized plasma spray of Baghdadite (BAG), a calcium silicate-based bioceramic, produced a coating that exhibited mechanical properties superior to gas-stabilized plasma sprayed hydroxyapatite (HAp). The BAG coating possessed higher hardness and elastic modulus under micro-

and nano-scale hardness testing, as well as improved scratch and wear resistance under identical conditions and applied loads.

Also, the BAG coating exhibited a homogeneous structure, resulting in a consistent behavior of hardness, elastic modulus, scratch and wear resistance throughout the coating cross section. Such behavior is more favorable than that of the HAp coating, which exhibited fluctuations in its mechanical properties.

Importantly, the BAG coating supports the attachment and proliferation of human osteoblast cells to a greater degree when compared with the HAp and possesses excellent gene expression capability.

In general, the BAG coating manufactured by the hybrid water-stabilized plasma process demonstrates (i) enhanced mechanical properties, and (ii) improved biological response; which highlights Baghdadite as a potential biomaterial coating for orthopedic implants.

Acknowledgement

We acknowledge support from the Australian Research Council (ARC). The Centre for Innovative BioEngineering is funded under the Industrial Transformation Training Centre (ITTC) scheme via Award IC170100022. Ang and Berndt acknowledge the support from ARC Industrial Transformation Training Centre (ITTC) scheme via Award IC180100005. The Czech Science Foundation project GA19-10246S are gratefully acknowledged. The authors would like to thank Mr. Andrew Moore for expert assistance in sample preparation.

Conflict of Interest

All authors declare that no conflicts of interest are present regarding the publication of this paper.

References

[1] C. Wu, J. Chang, A review of bioactive silicate ceramics, Biomedical Materials 8(3) (2013) 032001. https://doi.org/10.1088/1748-6041/8/3/032001

[2] Y. Zhou, C. Wu, Y. Xiao, The stimulation of proliferation and differentiation of periodontal ligament cells by the ionic products from $Ca_7Si_2P_2O_{16}$ bioceramics, Acta Biomaterialia 8(6) (2012) 2307-2316. https://doi.org/10.1016/j.actbio.2012.03.012

[3] H. Li, K. Xue, N. Kong, K. Liu, J. Chang, Silicate bioceramics enhanced vascularization and osteogenesis through stimulating interactions between endothelia cells and bone marrow stromal cells, Biomaterials 35(12) (2014) 3803-3818.https://doi.org/10.1016/j.biomaterials.2014.01.039

[4] G. Wang, S.-I. Roohani-Esfahani, W. Zhang, K. Lv, G. Yang, X. Ding, D. Zou, D. Cui, H. zreiqat, X. Jiang, Effects of Sr-HT-Gahnite on osteogenesis and angiogenesis by adipose derived stem cells for critical-sized calvarial defect repair, Scientific Reports 7(1) (2017) 41135. https://doi.org/10.1038/srep41135

[5] B.-C. Wu, S.-C. Youn, C.-T. Kao, S.-C. Huang, C. Hung, Jr., M.-Y. Chou, T.-H. Huang, M.-Y. Shie, The effects of calcium silicate cement/fibroblast growth factor-2 composite on osteogenesis

accelerator in human dental pulp cells, Journal of Dental Sciences 10(2) (2015) 145-153. https://doi.org/10.1016/j.jds.2013.12.003

[6] P.N. de Aza, F. Guitian, S. de Aza, Bioactivity of wollastonite ceramics: In vitro evaluation, Scripta Metallurgica et Materialia 31(8) (1994) 1001-1005. https://doi.org/10.1016/0956-716X(94)90517-7

[7] X. Liu, C. Ding, Z. Wang, Apatite formed on the surface of plasma-sprayed wollastonite coating immersed in simulated body fluid, Biomaterials 22(14) (2001) 2007-2012. https://doi.org/10.1016/S0142-9612(00)00386-0

[8] S. Fu, W. Liu, S. Liu, S. Zhao, Y. Zhu, 3D printed porous β-Ca2SiO4 scaffolds derived from preceramic resin and their physicochemical and biological properties, Science and Technology of Advanced Materials 19(1) (2018) 495-506. https://doi.org/10.1080/14686996.2018.1471653

[9] Y. No, J. Li, H. Zreiqat, Doped Calcium Silicate Ceramics: A New Class of Candidates for Synthetic Bone Substitutes, Materials 10(2) (2017) 153. https://doi.org/10.3390/ma10020153

[10] Z. Lu, G. Wang, I. Roohani-Esfahani, C.R. Dunstan, H. Zreiqat, Baghdadite Ceramics Modulate the Cross Talk Between Human Adipose Stem Cells and Osteoblasts for Bone Regeneration, Tissue Engineering Part A 20(5-6) (2014) 992-1002. http://dx.doi.org/10.1089/ten.tea.2013.0470

[11] T.C. Schumacher, E. Volkmann, R. Yilmaz, A. Wolf, L. Treccani, K. Rezwan, Mechanical evaluation of calcium-zirconium-silicate (baghdadite) obtained by a direct solid-state synthesis route, Journal of the Mechanical Behavior of Biomedical Materials 34 (2014) 294-301. https://doi.org/10.1016/j.jmbbm.2014.02.021

[12] Z. Zhu, Z. Sun, Z. Guo, X. Zhang, Luminescence of Ca3ZrSi2O9: Ce3+ blue phosphor with good thermal stability, Journal of Luminescence 207 (2019) 430-434. https://doi.org/10.1016/j.jlumin.2018.11.049

[13] P. S. Shashidhara, J. K. Thomas, Phase relations in the system CaO-SiO2-ZrO2 at 1573 K, Steel Research 65(10) (1994) 410-413. https://doi-org/10.1002/srin.199401185

[14] Y. Ramaswamy, C. Wu, A. Van Hummel, V. Combes, G. Grau, H. Zreiqat, The responses of osteoblasts, osteoclasts and endothelial cells to zirconium modified calcium-silicate-based ceramic, Biomaterials 29(33) (2008) 4392-4402. https://doi.org/10.1016/j.biomaterials.2008.08.006

[15] Y. Liang, Y. Xie, H. Ji, L. Huang, X. Zheng, Excellent stability of plasma-sprayed bioactive Ca3ZrSi2O9 ceramic coating on Ti–6Al–4V, Applied Surface Science 256(14) (2010) 4677-4681. https://doi.org/10.1016/j.apsusc.2010.02.071

[16] S. Sadeghpour, A. Amirjani, M. Hafezi, A. Zamanian, Fabrication of a novel nanostructured calcium zirconium silicate scaffolds prepared by a freeze-casting method for bone tissue engineering, Ceramics International 40(10, Part B) (2014) 16107-16114. https://doi.org/10.1016/j.ceramint.2014.07.039

[17] G. Róg, A. Kozłowska-Róg, M. Bućko, K. Haberko, Application of solid-state galvanic cells to the thermodynamic study of the CaO–SiO2–ZrO2 system, Solid State Ionics 176(9) (2005) 991-994. https://doi.org/10.1016/j.ssi.2004.11.020

[18] S.Y. Kwon, W.-Y. Kim, P. Hudon, I.-H. Jung, Thermodynamic modeling of the CaO-SiO2-ZrO2 system coupled with key phase diagram experiments, Journal of the European Ceramic Society 37(3) (2017) 1095-1104. https://doi.org/10.1016/j.jeurceramsoc.2016.10.011

[19] C.C. Berndt, F. Hasan, U. Tietz, K.P. Schmitz, A Review of Hydroxyapatite Coatings Manufactured by Thermal Spray, in: B. Ben-Nissan (Ed.), Advances in Calcium Phosphate Biomaterials, Springer Berlin Heidelberg, Berlin, Heidelberg, 2014, pp. 267-329. https://doi.org/10.1007/978-3-642-53980-0_9

[20] T. Tesar, R. Musalek, J. Medricky, J. Cizek, On growth of suspension plasma-sprayed coatings deposited by high-enthalpy plasma torch, Surface and Coatings Technology 371 (2019) 333-343. https://doi.org/10.1016/j.surfcoat.2019.01.084

[21] T. Tesar, R. Musalek, F. Lukac, J. Medricky, J. Cizek, V. Rimal, S. Joshi, T. Chraska, Increasing α-phase content of alumina-chromia coatings deposited by suspension plasma spraying using hybrid and intermixed concepts, Surface and Coatings Technology 371 (2019) 298-311. https://doi.org/10.1016/j.surfcoat.2019.04.091

[22] Hrabovsky, Water-stabilized plasma generators, Pure and Applied Chemistry, 1998, p. 1157. http://dx.doi.org/10.1351/pac199870061157

[23] J. Cizek, V. Brozek, T. Chraska, F. Lukac, J. Medricky, R. Musalek, T. Tesar, F. Siska, Z. Antos, J. Cupera, M. Matejkova, Z. Spotz, S. Houdkova, M. Kverka, Silver-Doped Hydroxyapatite Coatings

Deposited by Suspension Plasma Spraying, Journal of Thermal Spray Technology 27(8) (2018) 1333-1343. https://doi.org/10.1007/s11666-018-0767-2

[24] Y.J. No, I. Holzmeister, Z. Lu, S. Prajapati, J. Shi, U. Gbureck, H. Zreiqat, Effect of Baghdadite Substitution on the Physicochemical Properties of Brushite Cements, Materials 12(10) (2019) 1719. https://doi.org/10.3390/ma12101719

[25] ISO 4287:1997, Geometrical Product Specifications (GPS) - Surface texture: Profile method - Terms, definitions and surface texture parameters, International Organization for Standardization, 1997. https://www.iso.org/standard/10132.html (accessed 14 Septemper 2020).

[26] N. Otsu, A Threshold Selection Method from Gray-Level Histograms, IEEE Transactions on Systems, Man, and Cybernetics 9(1) (1979) 62-66. https://doi.org/10.1109/TSMC.1979.4310076

[27] A.S.M. Ang, C.C. Berndt, A review of testing methods for thermal spray coatings, International Materials Reviews 59(4) (2014) 179-223. https://doi.org/10.1179/1743280414Y.0000000029

[28] P. Ostojic, C.C. Berndt, The variability in strength of thermally sprayed coatings, Surface and Coatings Technology 34(1) (1988) 43-50. https://doi.org/10.1016/0257-8972(88)90087-4

[29] W.C. Oliver, G.M. Pharr, An improved technique for determining hardness and elastic modulus using load and displacement sensing indentation experiments, Journal of Materials Research 7(6) (1992) 1564-1583. https://doi.org/10.1557/JMR.1992.1564

[30] P. Sudharshan Phani, W.C. Oliver, A critical assessment of the effect of indentation spacing on the measurement of hardness and modulus using instrumented indentation testing, Materials & Design 164 (2019) 107563. https://doi.org/10.1016/j.matdes.2018.107563

[31] L. Sun, C.C. Berndt, K.A. Gross, A. Kucuk, Material fundamentals and clinical performance of plasma-sprayed hydroxyapatite coatings: A review, Journal of Biomedical Materials Research 58(5) (2001) 570-592. https://doi.org/10.1002/jbm.1056

[32] H.M. Al-Hermezi, D. McKie, A.J. Hall, Baghdadite, a new calcium zirconium silicate mineral from Iraq, Mineralogical Magazine 50(1) (1986) 119-123. doi: 10.1180/minmag.1986.050.355.15

[33] C.Y. Tan, R. Singh, Y.C. Teh, Y.M. Tan, B.K. Yap, The Effects of Calcium-to-Phosphorus Ratio on the Densification and Mechanical Properties of Hydroxyapatite Ceramic, International Journal of Applied Ceramic Technology 12(1) (2015) 223-227. https://doi.org/10.1111/ijac.12249

[34] D.Q. Pham, C.C. Berndt, U. Gbureck, H. Zreiqat, V.K. Truong, A.S.M. Ang, Mechanical and chemical properties of Baghdadite coatings manufactured by atmospheric plasma spraying, Surface and Coatings Technology (2019) 124945. https://doi.org/10.1016/j.surfcoat.2019.124945

[35] K.A. Gross, S. Saber-Samandari, K.S. Heemann, Evaluation of commercial implants with nanoindentation defines future development needs for hydroxyapatite coatings, Journal of Biomedical Materials Research Part B: Applied Biomaterials 93B(1) (2010) 1-8. https://doi.org/10.1002/jbm.b.31537

[36] K.A. Gross, C.C. Berndt, V.J. Iacono, M. Implants, Variability of hydroxyapatite-coated dental implants, The International Journal of Oral & Maxillofacial Implants 13(5) (1998), 601-610.

[37] H. Zhou, S.B. Bhaduri, 3 - The translatory aspects of calcium phosphates for orthopedic applications, in: L. Yang, S.B. Bhaduri, T.J. Webster (Eds.), Biomaterials in Translational Medicine, Academic Press2019, pp. 37-55. https://doi.org/10.1016/B978-0-12-813477-1.00003-7

[38] R.B. Heimann, Thermal spraying of biomaterials, Surface and Coatings Technology 201(5) (2006) 2012-2019. https://doi.org/10.1016/j.surfcoat.2006.04.052

[39] A. Najafinezhad, M. Abdellahi, H. Ghayour, A. Soheily, A. Chami, A. Khandan, A comparative study on the synthesis mechanism, bioactivity and mechanical properties of three silicate bioceramics, Materials Science and Engineering: C 72 (2017) 259-267. https://doi.org/10.1016/j.msec.2016.11.084

[40] C.K. Lin, C.C. Berndt, Statistical analysis of microhardness variations in thermal spray coatings, Journal of Materials Science 30(1) (1995) 111-117. https://doi.org/10.1007/BF00352139

[41] A.S.M. Ang, C.C. Berndt, M.L. Sesso, A. Anupam, P. S, R.S. Kottada, B.S. Murty, Plasma-Sprayed High Entropy Alloys: Microstructure and Properties of AlCoCrFeNi and MnCoCrFeNi, Metallurgical and Materials Transactions A 46(2) (2015) 791-800. https://doi.org/10.1007/s11661-014-2644-z

[42] Q.D. Pham, C.C. Berndt, A. Sadeghpour, H. Zreiqat, P.-Y. Wang, S.M.A. Ang, Mechanical Properties of Strontium–Hardystonite–Gahnite Coating Formed by Atmospheric Plasma Spray, Coatings 9(11) (2019). https://doi.org/10.3390/coatings9110759

[43] S.B. Goodman, The effects of micromotion and particulate materials on tissue differentiation: Bone chamber studies in rabbits, Acta Orthopaedica Scandinavica 65(sup258) (1994) 1-43. https://doi.org/10.3109/17453679409155227

[44] K.F. Wang, C.C. Zhou, Y.L. Hong, X.D. Zhang, A review of protein adsorption on bioceramics, Interface Focus 2(3) (2012) 259-277. https://doi.org/10.1098/rsfs.2012.0012

Appendices

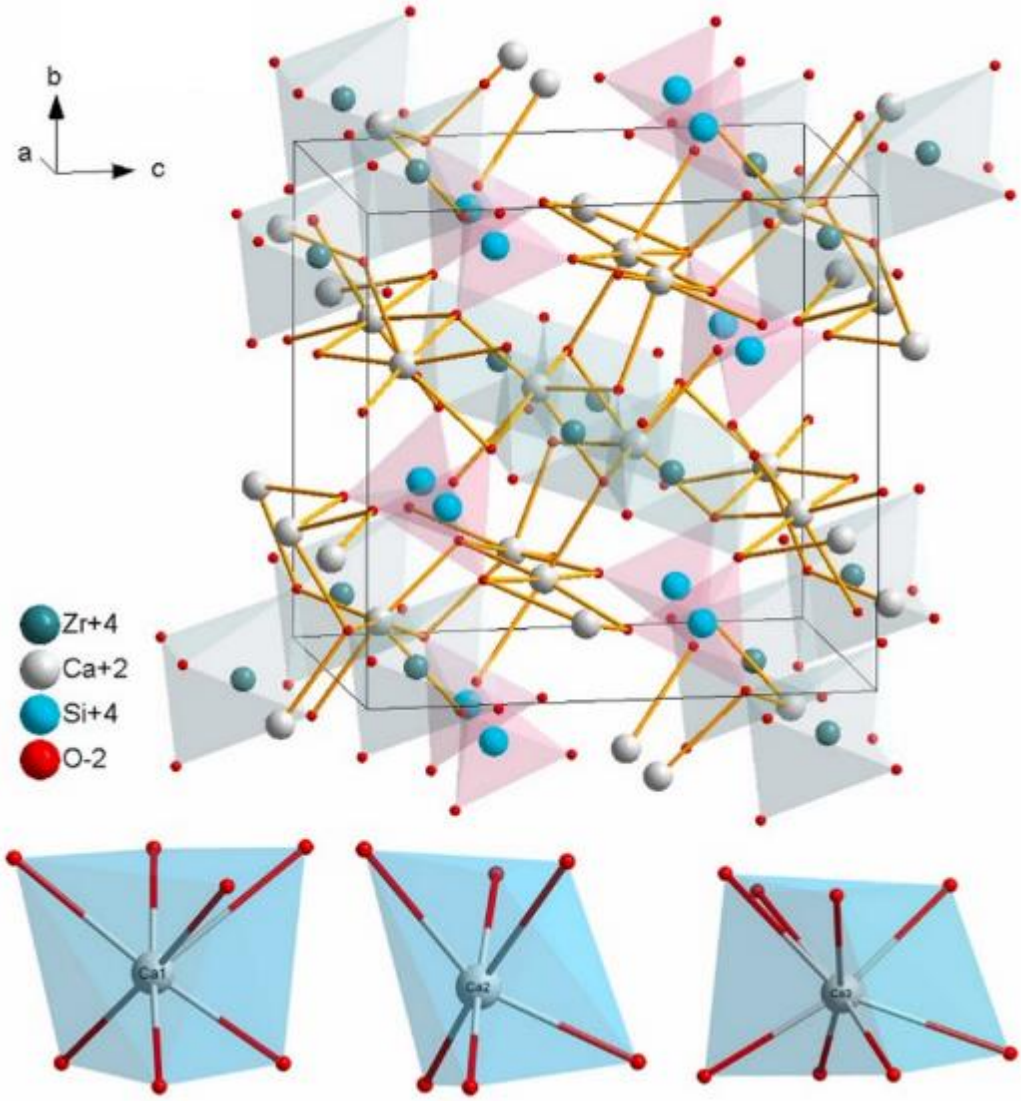

Fig. A. 1. Crystal structure of Baghdadite. Adapted from [8]

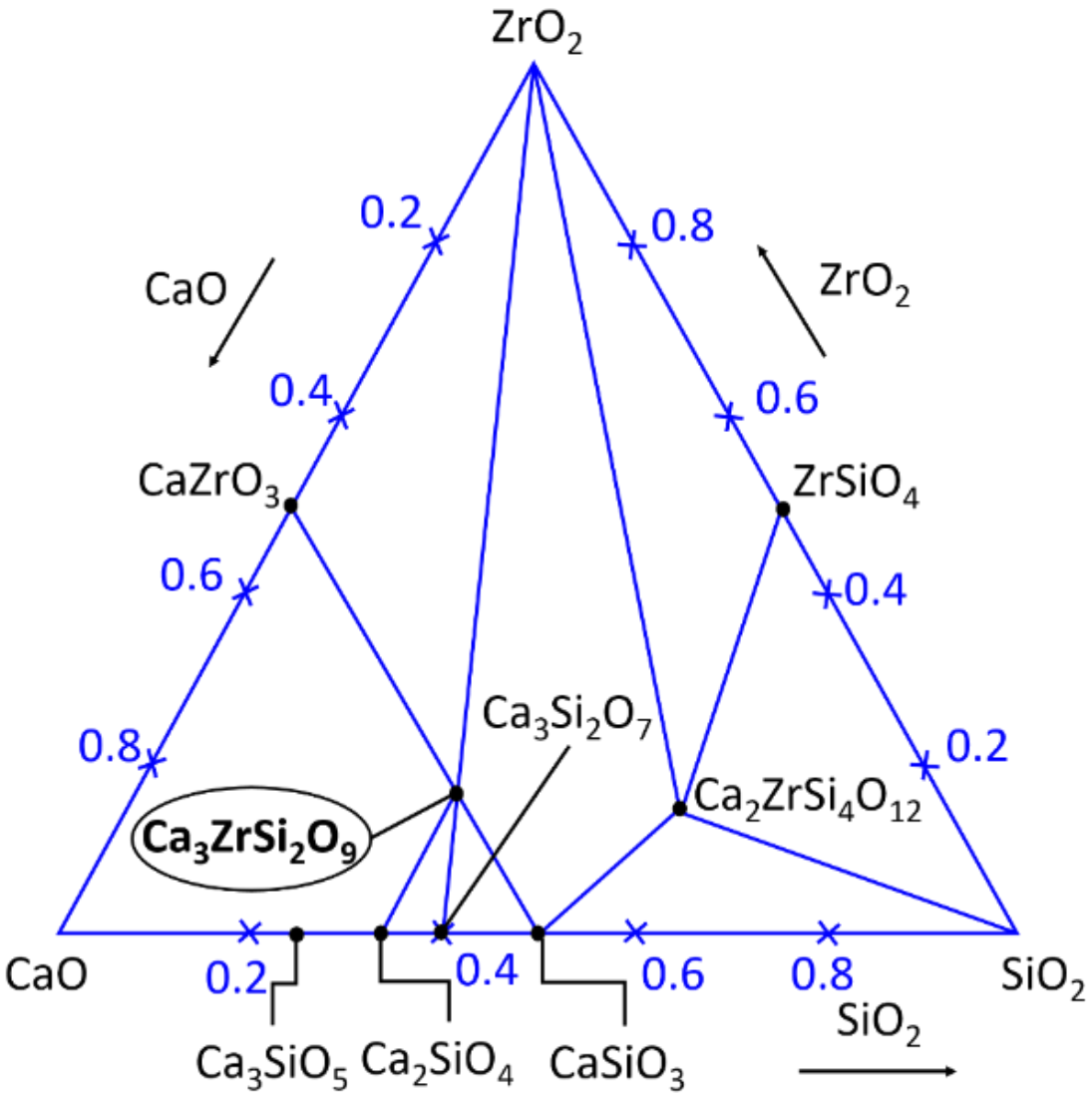

Fig. A. 2. Compositions in the $CaO-ZrO_2-SiO_2$ phase diagram studied at 1573 K with two ternary compounds of $Ca_3ZrSi_2O_9$ (BAG) and $Ca_2ZrSi_4O_{12}$ presented in the system. Adapted from [9].

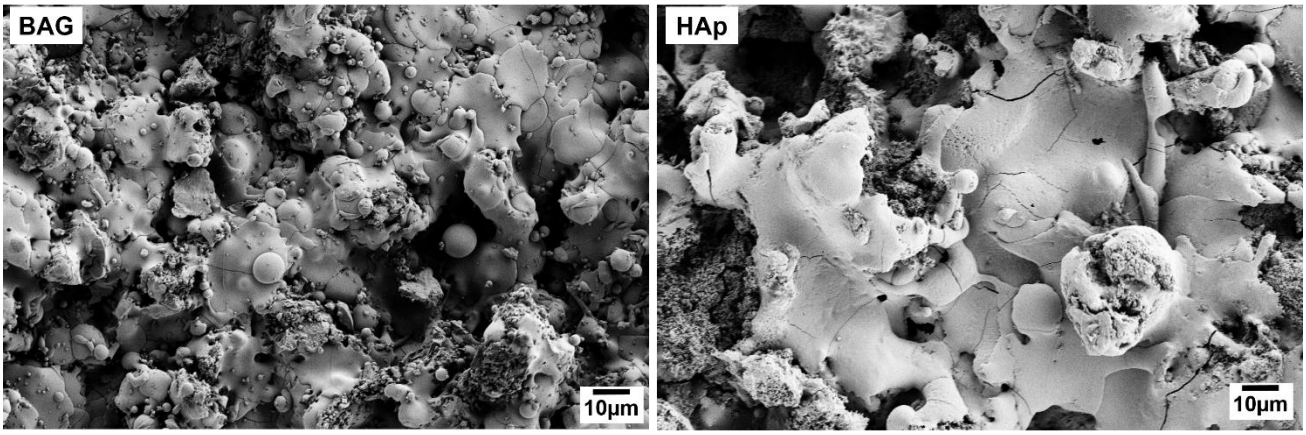

Fig. A. 3. Top surface of the BAG and the HAp coating.

Credit Authorship Contribution Statement

Duy Quang Pham: Conceptualization, Methodology, Software, Validation, Formal Analysis, Investigation, Data Curation, Writing - Original Draft, Visualization

Christopher C. Berndt: Conceptualization, Resources, Writing – Review & Editing, Visualization, Supervision, Funding Acquisition

Jan Cizek: Methodology, Resources, Writing – Review & Editing

Uwe Gbureck: Methodology, Resources, Review & Editing

Hala Zreiqat: Conceptualization, Resources, Writing – Review & Editing, Funding Acquisition,

Zufu Lu: Methodology, Resources, Investigation, Writing – Review & Editing

Andrew Siao Ming Ang: Conceptualization, Methodology, Investigation, Resources, Writing – Review & Editing, Visualization, Supervision, Funding Acquisition